Planetary Circulations: 3. The Terrestrial Quasi-Geostrophic Regime

GARETH P. WILLIAMS

Geophysical Fluid Dynamics Laboratory/NOAA, Princeton University, Princeton, NJ 08540

(Manuscript received 29 December 1978, in final form 2 April 1979)

ABSTRACT

The characteristics of the two-level quasi-geostrophic model are evaluated for a wide range of parameters in the terrestrial domain. Flow form is determined primarily by β (the Coriolis gradient) and by τ_D (the time scale of the surface drag), acting through the influence of Rhines' transitional wavenumber $k_\beta = (\beta/2\tilde{U})^{1/2}$, where $\tilde{U}^2$ is the barotropic energy level. Two extreme types of circulation occur: jets when k_β is large, and gyres when wave propagation and drag are negligible.

The present terrestrial circulation, in its quasi-geostrophic representation, is extremely efficient: the system can cope with increased heating rates without a significant rise in the pole-to-equator temperature differential. Although each hemisphere is, on occasion, near to transforming into a double-jet state, multi-jet circulations—corresponding to those in the Jovian regime—occur more readily at higher rotation rates. For the existing circulation to switch to a gyre form requires a large, unrealizable drop in surface drag.

1. Introduction

To classify the character (and Jovian relationship) of the Earth's atmospheric circulation, we need to know what forms of planetary circulation can occur and how stable each one is. A limited solution to this problem can be obtained by evaluating the parametric variation of the two-layer quasi-geostrophic model. This model describes (to first order) how the rotation rate, static stability, surface drag and heating rate shape the circulation of a rapidly rotating atmosphere. Although it excludes or oversimplifies many of the complex processes controlling the climate and its variability, the description it provides suffices for preliminary questions concerning *extreme* changes in circulation pattern.

The main parameter determining the *barotropic* characteristics is the Coriolis gradient β whose value specifies the transitional wavenumber $k_\beta = (\beta/2\tilde{U})^{1/2}$ separating the wave and turbulent scales of the circulation (Rhines, 1975). Because k_β is large for Jupiter, multiple, highly zonal jets prevail in that atmosphere (Williams, 1978, 1979). For Earth the wave transition occurs at a scale where the surface drag is equally influential, and to disentangle these two effects we have to evaluate how the circulation varies as a function of β and τ_D.

The *baroclinic* characteristics are mainly decided by the Rossby deformation wavenumber k_ρ. Although the circulations are often turbulent, the results of linear instability theory remain valid as regards the scale selectivity of the baroclinic eddies (Phillips, 1954; Stone, 1969) and the longitudinal localization of energy conversion (Thacker, 1976; Merkine, 1977); the localized instability of ultra-long baroclinic waves has been suggested as an explanation of Jupiter's Great Red Spot (Williams, 1979).

To determine the parametric variability of the two-level quasi-geostrophic model, we evaluate 1) the computational effect of limiting the domain size (Section 2); 2) the "basic" circulation, i.e., the circulation occurring at parameter values appropriate to the present terrestrial state (Section 3); 3) the effect of varying the surface drag, the rotation rate and static stability (Sections 4–6). Finally, we examine the response of the basic quasi-geostrophic circulation to increases in the heating rate, and deduce conditions for a transition to a gyre form (Section 7). The reader is referred to Part 2 for details of the quasi-geostrophic model and to Table 1 for the parameter values used in the calculations. For convenience, the main items of the notation are repeated below:

x	prograde longitudinal coordinate ($=0, X$)
y	poleward latitudinal coordinate ($=0, Y$)
f_0	Coriolis term
β	northward gradient of Coriolis term
a	planetary radius
Ω	planetary rotation rate
R	specific gas constant
T	temperature
ΔT	temperature difference between pole and equator

TABLE 1. Earth regime cases. Constant parameter values: $\Omega_E = 0.73 \times 10^{-4}$ s^{-1}, $f_E = 10^{-4}$ s^{-1}, $\beta_E = 0.16 \times 10^{-7}$ s^{-1} km^{-1}, $R = 0.29 \times 10^{-3}$ km^2 s^{-2} K^{-1}, $a = 6000$ km, $Y = 10^4$ km, $Y/\Delta y = 64$, $h = 8$ km. Linear heating function.

								Axisymmetric stage					Final phase					
Case	γ^2 (s^2 km^{-2})	f_0/f_E β/β_E	τ_D (10^5 s)	H_a (10^{-9} km^2 s^{-3})	X (10^3 km)	$X/\Delta x$	ν (km^2 s^{-1})	Δt (10^3 s)	Total time (days)	ΔT (°K)	U_1 (m s^{-1})	U_3 (m s^{-1})	Δt (10^3 s)	Total time (days)	ΔT (°K)	U_1 (m s^{-1})	U_3 (m s^{-1})	$-2\hat{\psi}_L$ (km^2 s^{-1})
A1	150	1	5[c]	1	6	64	0.10	3.5	81	40.0	10.4	0.6	1.0	412	51.7	31.3	20.8	149
A2	150	1	2.5[p]	1	24	128	0.05	10	115	52.7	23.5	7.3	1.2	283	39.7	31.9	20.9	230
A3	150	1	2.5[p]	4 → 8	24	128	0.05	10	58	52.7	23.5	7.3	0.7	353	67.0	73.3	56.8	389
A4	150	1	20[c]	4	24	128	0.05	10	115	54.1	18.9	2.3	0.7	133	54.4	83.5	72.5	290
B1	150	1	∞	0.2 → 0.5	24	128	0.10	5	57	28.7	4.3	4.3	1.2	490	51.3	26.9	21.0	0
B2	150	1	∞	1	24	128	0.05	7	81	40.7	6.1	6.1	0.9	317	57.2	70.8	59.3	0
C1	150	4	5[c]	1	24	256	0.05	9	104	55.0	3.7	0.4	1.5	207	85.5	19.9	16.1	60
C2	150	4	∞	0.5	24	256	0.05	18	207	53.0	2.0	2.0	1.2	317	88.5	18.9	17.0	0
D1	600	1	2.5[p]	1	24	128	0.05	4	46	24.0	9.9	2.7	1.5	275	22.7	26.1	20.0	139
D2	600	1	∞	1	24	128	0.05	3	35	18.8	2.8	2.8	0.9	221	22.5	80.3	75.3	0
D3	55	1	5[c]	1	30	128	0.10	11	253	97.0	29.1	12.6	1.2	239	69.0	38.8	22.9	204

Suffixes in τ_D column denote Phillips or Charney forms of ζ_4 used.

ν horizontal small-scale diffusion coefficient
H_a amplitude of non-adiabatic heating rate function
H_a^* nondimensional heating rate [$=H_a/10^{-9}$ km^2 s^{-3}]
h scale height
γ^2 inverse static stability parameter
s relative static stability factor [$=150/\gamma^2$]
λ^2 Froude parameter [$=f_0^2\gamma^2$]
τ_D time scale of surface drag
q potential vorticity
ζ vorticity [$=\nabla^2\psi$]
ψ geostrophic streamfunction [$u = -\psi_y$, $v = \psi_x$]
u, v zonal and meridional velocities
w vertical velocity
U rms speed, averaged over domain
$(\bar{\ })$ zonal mean [$=X^{-1}\int_0^X (\ )dx$]
$(\ )'$ zonal eddy
$(\hat{\ })$ baroclinic component {$=[(\ )_1 - (\ )_3]/2$, difference between values at p_1, p_3 levels}
$(\tilde{\ })$ barotropic component {$=[(\ )_1 + (\ )_3]/2$, average of values at p_1, p_3 levels}
K, P domain-mean kinetic and potential energies
$\{AB\}$ domain-mean energy exchange from A to B. Q, F, D, I denote conversions related to heating, lateral diffusion, surface drag and interface stress.

2. The geometrical effect

In the original experiment designed by Phillips (1956), the width of the β-plane was chosen (because of computational limitations) to be a minimal value equal to L_c, the preferred critical wavelength predicted by linear theory (Table 2). To examine how severely this choice restricts the nonlinear development of the solution, we begin by recomputing the same case (A1 in Table 1). The only differences occur in the formulation of the surface drag, in the boundary and computational conditions (see Part 2), and in the resolution and internal dissipation.

The circulation A1 evolves through a spinup phase involving four separate stages (Table 3): 1) the baroclinic instability of the axisymmetric flow and its occlusion at 35–46 days; 2) the baroclinic instability of the single jet at 70 days; 3) the transition from one to two jets at 80–180 days; and 4) the statistical equilibration of the double-jet state.

a. Instability of the axisymmetric state

As shown in Fig. 1 the initial development of the perturbed unstable axisymmetric state (see Table 1) displays the features and correlations of linear instability theory (Phillips, 1954): temperature-lagging geopotential, a latitudinal phase-line variation synonymous with momentum convergence, eastward wave propagation at approximately 10^3 km day^{-1}, vortex stretching and a triple-cell circulation. When the instability occludes (~45 days), the jet becomes more zonal and the triple-cell structure disappears.

TABLE 2. Minimum values of critical length scale, shear and temperature differential, $L_c = 2\pi 2^{1/4}/\gamma f_0$, $\hat{u}_c = \beta/2\gamma^2 f_0^2$, $\Delta T_c = \beta Y/R f_0 \gamma^2$, as a function of parameters [after Phillips (1954)].

Case class	f_0/f_E	γ^2 (s^2 km^{-2})	s	L_c (10^3 km)	$2\hat{u}_c$ (m s^{-1})	ΔT_c (K)
A, B	1	150	1	6	10	35
C	4	150	1	1.5	2.5	35
D	1	600	¼	3	2.5	9
D	1	55	3	10	30	90

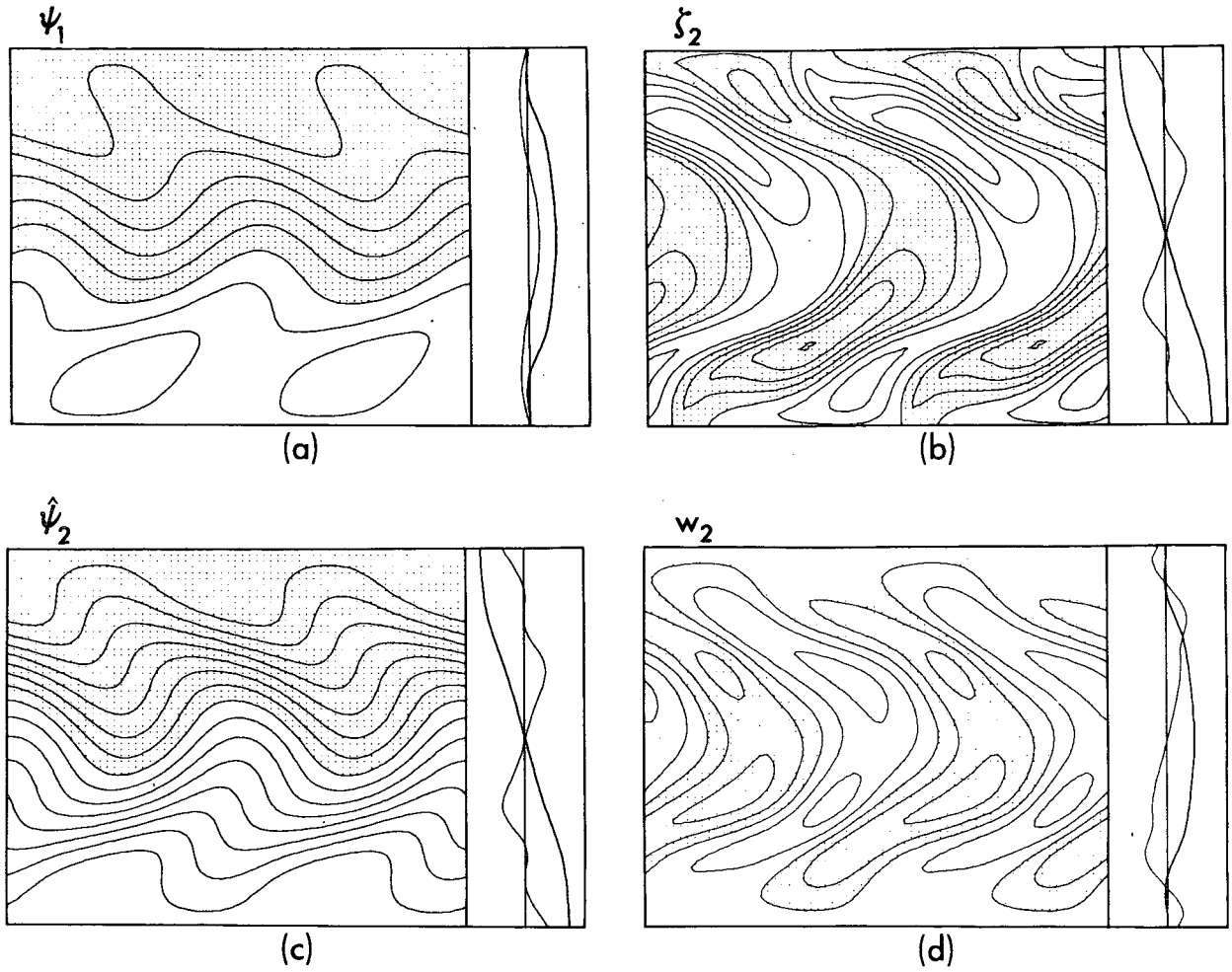

FIG. 1. Case A1 at 40 days. Basic fields and profiles. Fields are ψ_1, ζ_2, $\hat{\psi}_2$, w_2 in (a)–(d), respectively; indices denote pressure level, ordinate $y = 0, Y$, abscissa $x = 0, 2X$ (integration domain is repeated twice in x for display purposes in A1 only). Fields are denoted by contour interval, e.g., $\Delta\psi_1$ in (a), with zero and negative values shaded by a selection of grid points. On the right-hand side are latitudinal profiles of some zonal mean quantities, plotted in terms of amplitudes denoted by asterisked values and with zero values at the center; heavy line profile is listed first. Same notation is used in all figures.

(a) $\Delta\psi_1 = 20$ km^2 s^{-1}, $u_1^* = 62$ m s^{-1}, $u_3^* = 62$ m s^{-1}
(b) $\Delta\zeta_2 = 1 \times 10^{-5}$ s^{-1}, $T_2^* = 35$ K, $w_2^* = 1 \times 10^{-5}$ km s^{-1}
(c) $\Delta\hat{\psi}_2 = 10$ km^2 s^{-1}, $T_2^* = 35$ K, $w_2^* = 1 \times 10^{-5}$ km s^{-1}
(d) $\Delta w_2 = 1 \times 10^{-5}$ km s^{-1}, $u_1^* = 62$ m s^{-1}, $\zeta_2^* = 3 \times 10^{-5}$ s^{-1}.

b. Instability of the single jet

The next instability, that of a mean zonal flow with latitudinal shear (as shown in Fig. 2), produces (~69 days) eddies with a bimodal meridional structure and a scale determined by $\bar{u}(y)$. The partitioning of vortices of like sign, in the manner described by Kuo (1951) and the E1 solution of Part 1, enhances momentum convergence into the jet.

c. Transition to a double jet

During the period from 80 to 100 days, when potential energy release is relatively weak (Table 3), the jet and baroclinicity axis shift poleward. The onset of another instability (~115 days) initiates a complex change in the flow structure: large anticyclonic gyres arise that cause the jet to vacillate and transfer momentum equatorward to create a second westerly flow (Fig. 3).

d. Instability of the double jet

When the two jets become fully baroclinically-unstable and of comparable amplitude at ~207 days, the new jet lags the original one by $\pi/4$, but later, as the flow equilibrates (Fig. 4), the lag increases to $\pi/2$. The final phase relationship indi-

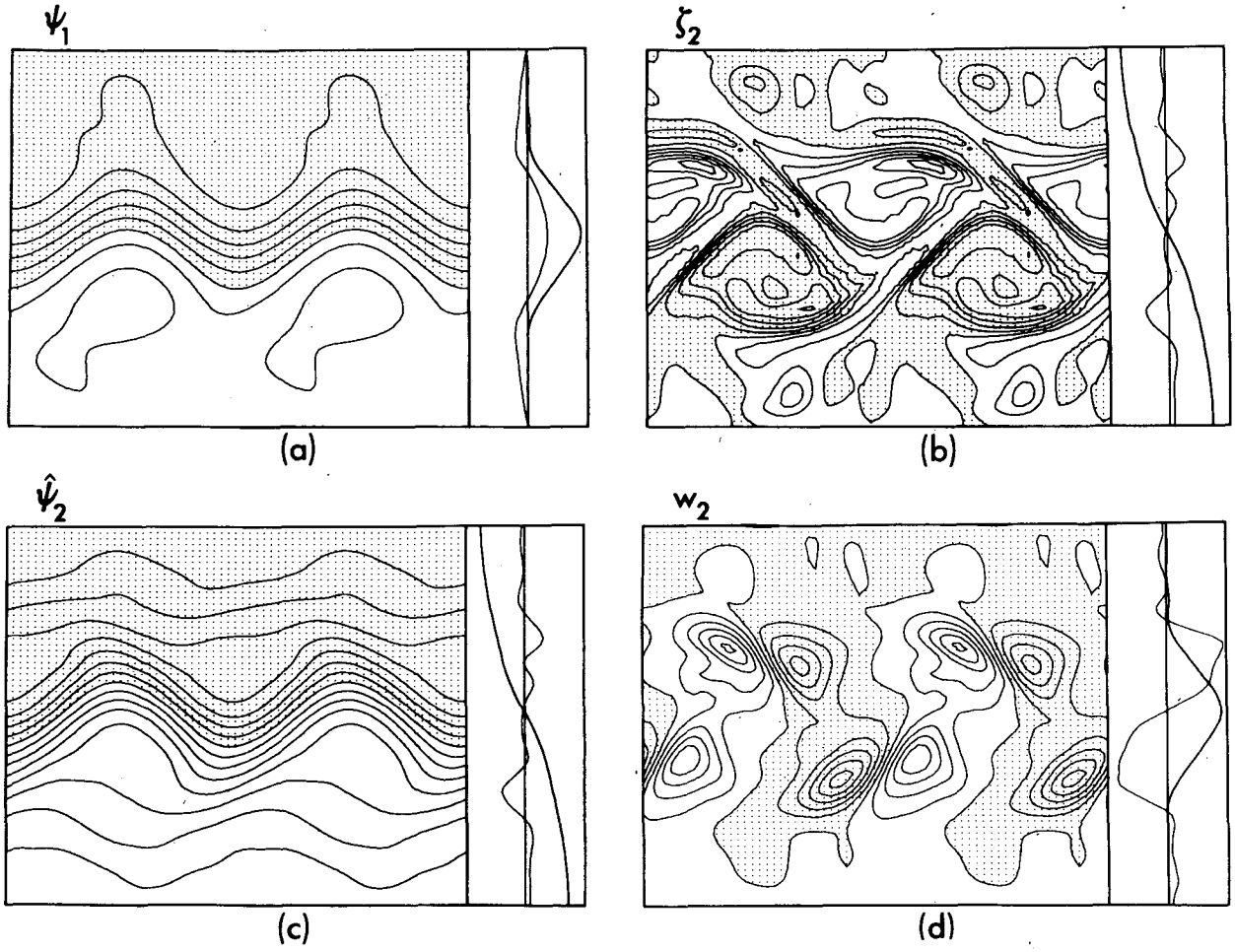

FIG. 2. Case A1 at 60 days. Notation and contour intervals as Fig. 1.

TABLE 3. Case A1. Instantaneous global means of energy and energy conversion. Units are 10^{-6} km^2 s^{-2} for K', $\bar{K}$, P'; 10^{-5} km^2 s^{-2} for $\bar{P}$; 10^{-12} km^2 s^{-3} for conversion terms; m s^{-1} for the rms velocities U_1, U_3, and K for ΔT. Time measured from end of axisymmetric spinup.

Days	ΔT	$-2\bar{\psi}_L$	U_1	U_3	K'	$\bar{K}$	P'	$\bar{P}$	$\{Q\bar{P}\}$	$\{\bar{P}P'\}$	$\{P'K'\}$	$\{K'\bar{K}\}$	$\{\bar{P}\bar{K}\}$	$\{\bar{K}D\}$	$\{K'D\}$	$\{\bar{K}F\}$	$\{K'F\}$	$\{\bar{P}F\}$	$\{P'F\}$
0	40.0	84	10.4	1.6	0	56	0	106	325	0	0	0	21	3	0	3	0	4	0
23	49.8	115	13.6	1.6	0	93	0	169	410	0	0	0	27	3	0	2	0	34	0
37	54.9	132	16.6	5.3	20	121	13	209	456	239	161	33	8	2	6	3	7	42	4
46	48.8	138	27.1	15.9	104	359	34	189	431	706	643	509	−78	149	48	36	91	39	18
57	44.5	135	25.6	10.5	31	337	13	218	453	62	27	−40	−27	68	8	33	16	50	5
69	51.3	137	29.4	19.1	167	351	82	218	461	814	721	197	−73	126	39	43	70	46	29
92	45.5	141	36.6	23.8	225	603	98	167	391	143	178	−28	−48	271	40	76	118	48	37
115	50.2	139	31.9	19.8	178	416	101	175	407	1048	945	657	−246	148	24	58	77	50	34
126	51.7	143	32.6	23.7	308	325	120	165	402	537	587	677	−104	128	73	41	118	42	38
150	54.0	149	32.3	20.1	182	430	94	155	384	285	212	143	−68	158	23	66	82	53	33
172	58.1	158	29.8	17.6	154	346	96	177	415	485	394	231	−77	101	15	55	64	57	33
207	60.2	169	31.5	19.0	189	372	100	181	419	504	429	280	−82	117	24	61	79	58	37
218	57.4	170	33.0	22.0	283	340	138	173	412	813	732	372	−78	126	44	53	120	49	52
230	54.9	167	35.1	23.5	306	415	137	151	384	630	523	97	−83	176	47	68	140	47	54
252	52.8	161	33.3	22.4	313	316	147	141	372	484	403	159	−67	119	40	50	135	42	56
275	51.2	154	32.2	22.0	312	268	146	134	363	393	349	181	−47	95	42	42	133	39	55
321	50.8	148	30.3	20.5	275	235	131	132	361	404	368	243	−53	76	37	36	116	38	50
367	51.4	148	30.5	20.3	263	259	121	133	360	501	454	268	−60	85	42	41	115	40	46
412	51.7	149	31.3	20.8	267	286	122	132	358	577	486	260	−75	96	44	47	117	42	46

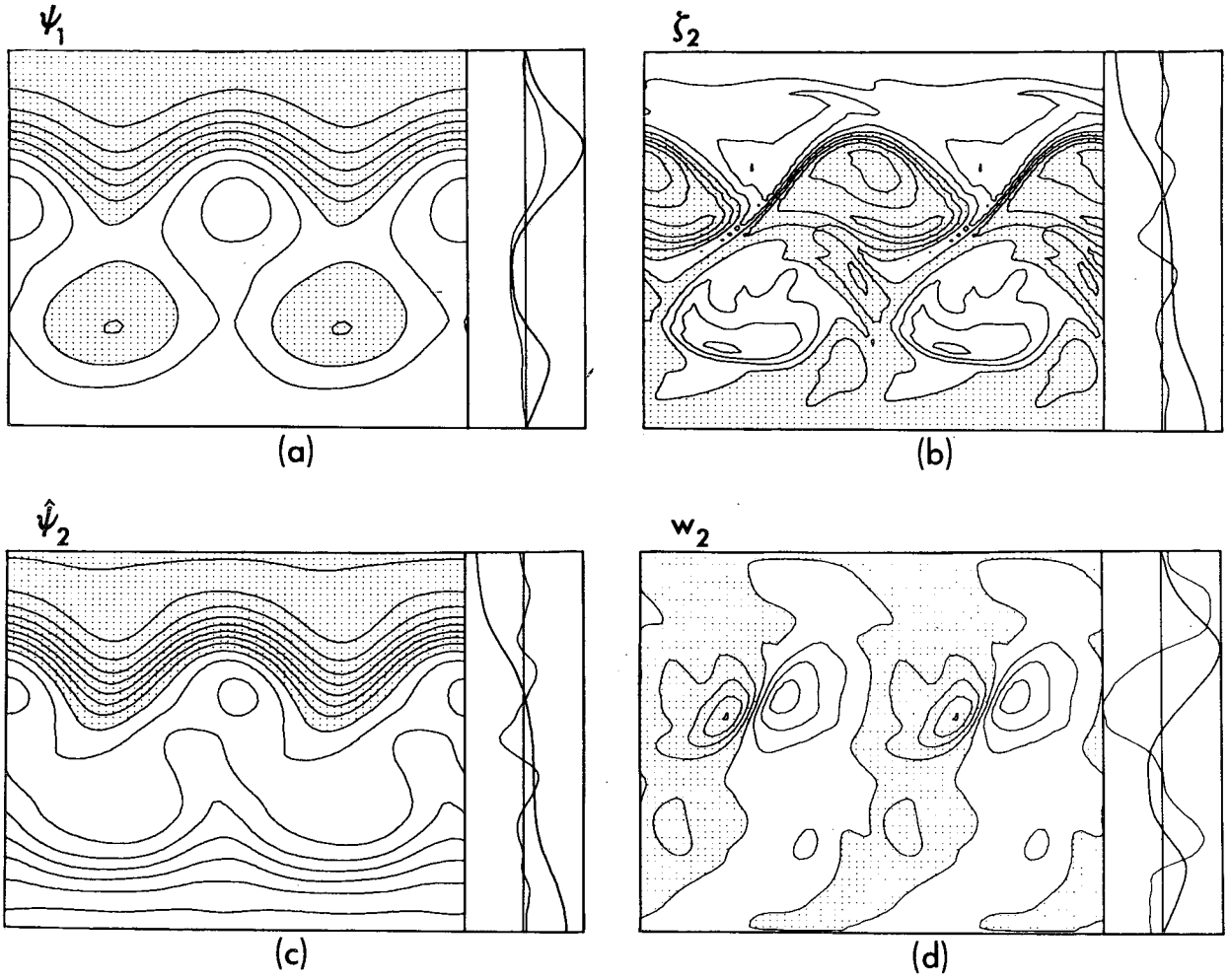

FIG. 3. Case A1 at 138 days. Notation and contour intervals as Fig. 1, but with $\Delta w_2 = 1.5 \times 10^{-5}$ km s^{-1} and $\Delta\zeta_2 = 1.5 \times 10^{-5}$ s^{-1}.

cates that potential energy is released mainly by the $k_x = 1$, $k_y = 1$ mode. The prevalence of this wave is also reflected by a meridional flow consisting of two sets of triple cells.

e. Energy transformations

The energy conversion rates $\{\bar{P}P'\}$, $\{P'K'\}$, $\{K'\bar{K}\}$ are (with minor exceptions) positive throughout the period of calculation, while the exchange $\{\bar{P}\bar{K}\}$ is negative (Table 3). This agrees with the standard picture of a jet maintained by eddy transports and equilibrated by the meridional circulation. The only negative values of $\{\bar{P}P'\}$ occur just after the initial jet moves poleward and the transition to a double jet begins (at 117 days).

f. Discussion

The two unexpected items in the A1 solution—the steady wave form of the final state and the transition from one to two jets—are consistent with the theory of barotropic wave-wave instabilities (Baines, 1976): the steadiness occurs because energy is released via a mode that is barotropically stable and noncascading, while the number of jets alters because the original configuration is barotropically unstable. Recalculating A1 with Y reduced to 6000 km produces a stable single-jet flow.

On Earth, the quasi-geostrophic region can vary from 6000 to 10 000 km, depending on the strength of the Hadley circulation. When the tropical regime is weak (as in the winter hemisphere) or when the extratropical energy level is low (as in the summer hemisphere), the ratio Y/L_β increases—where $L_\beta = \pi(2\bar{U}/\beta)^{1/2}$ is the width of jets formed by the Rhines effect—and a second jet becomes possible. Extreme variations in flow pattern are symptomatic of an atmosphere in a transitional state. A factor working against the emergence of a double jet in the manner described by A1 is the long time-scale of

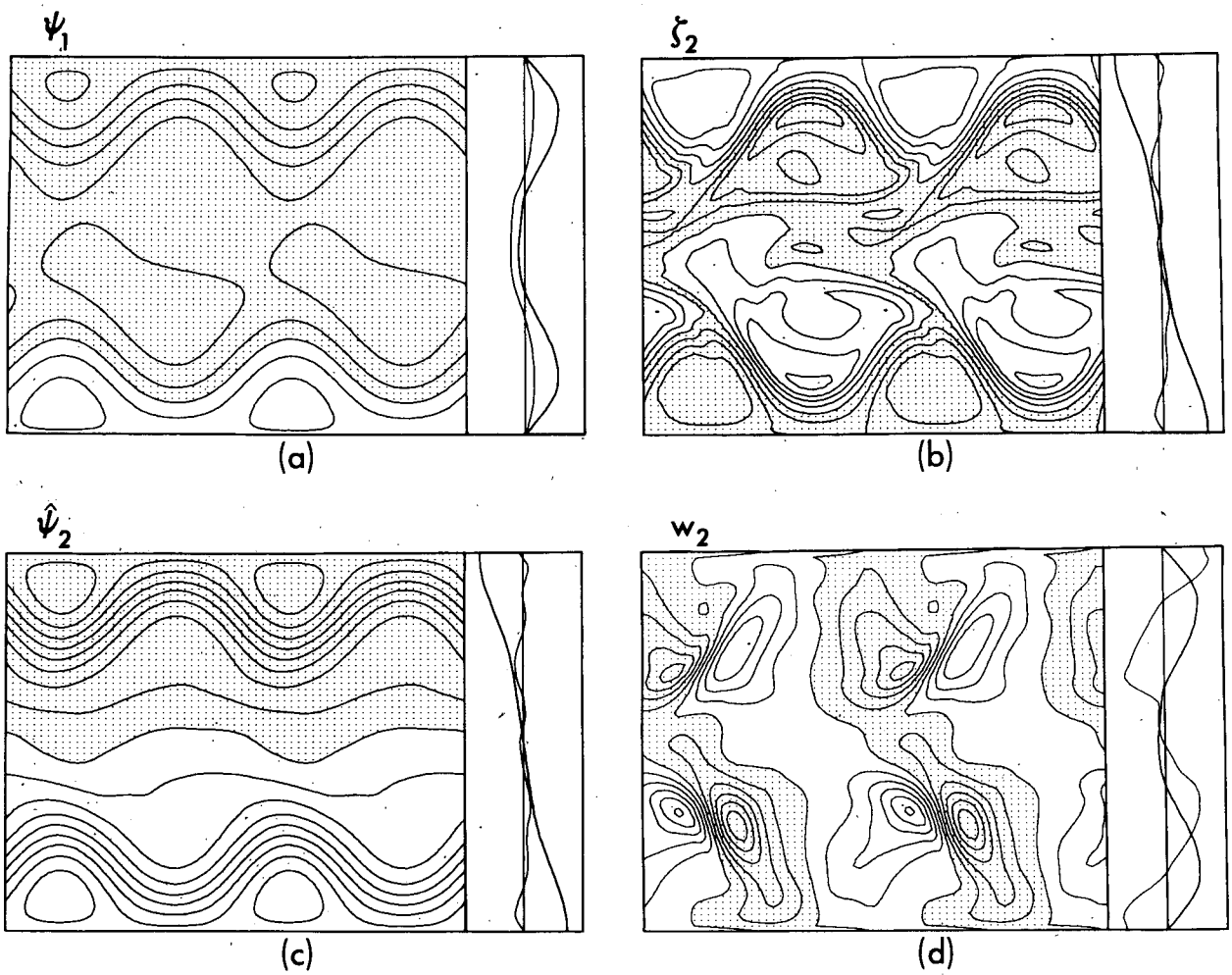

FIG. 4. Case A1 at 389 days. Notation and contour intervals as Fig. 1, but with $\Delta w_2 = 0.5 \times 10^{-5}$ km s^{-1}.

the transition—over such a lengthy period seasonal variations are more important. Furthermore, because of the spectral limitations of flow in an $X = L_c$ domain, the solution has uncertain physical applicability; additional solutions indicate that $X \geq 4\,L_c$ is preferable for producing nonlinear exchanges relevant to the atmosphere.

3. The basic circulation

When the integration domain is large enough to allow full nonlinearity, i.e., when X ($=4L_c$) is comparable to the Earth's circumference, the resulting circulation (A2) is as realistic as this model allows (Figs. 6–8).

The flow rapidly develops, from an initial state that complies with linear theory in its choice of preferred wavelength ($k_x = 4$, Fig. 6c), into a meandering jet that occasionally produces a cutoff low-pressure system (Fig. 7). This form persists throughout the integration and equilibrates with $\Delta T \approx 40$°K, $U_1 \approx 30$ m s^{-1} and three meridional-cells (Fig. 8).

Although k_ρ remains the dominant eddy wavenumber [in a k^{-4} spectrum (Fig. 5a)], energy conversion is strongly localized in longitude and appears to be related to the spatial type of baroclinic instability (Fig. 8c). This instability occurs when $\hat{U} > \sqrt{2}\hat{U}$ (Thacker, 1976), a condition which A2 marginally realizes. The conversion is strongly localized in time also, but only during the spinup phase; later it occurs more continuously, producing an irregular cycle with a time scale of the order of a month (Table 4).

To compare other forms of circulation with that of A2, we define the following morphological terms: 1) a flow is "jet-like" when momentum is latitudinally concentrated; 2) a jet is "zonal" when it flows mainly west-east; 3) a jet is "azonal" when it has a substantial north-south flow over its entire length; 4) a jet is "irregular" or "meandering" if the azonality is strongly x dependent; and 5) a flow is

"gyre-like" when the north-south flow equals or exceeds that in the west-east direction. A circulation is also described by the shape of its spectrum and this depends on the relative importance of the processes acting at the wavenumbers k_ρ, k_β and k_D $[\sim(U_4\tau_D)^{-1}]$—see Fig. 5.

Given that realistic circulations such as A2 can be produced, the model can be used to answer questions that may be raised about the terrestrial circulation: 1) is the form of motion unique or stable; 2) what role do processes represented by the β, τ_D and λ^2 parameters play in determining it; 3) can jets with less-irregularity and azonality be produced; 4) can multiple jets occur; and 5) when is energy conversion localized? These issues will be explored in the following sections.

4. Omitting drag: Energy-level effect in k_β

The surface drag, idealized by a term having barotropic and baroclinic components $(-\tilde{\zeta}/\tau_D, +\hat{\zeta}/\tau_D)$, acts in three ways in a circulation: 1) it helps define the value of the transitional wavenumber k_β by determining the amplitude of the motion; 2) its barotropic part $-\tilde{\zeta}/\tau_D$ extracts energy from the peak of the spectrum and prevents an accumulation in the largest scales [see Lilly (1972) for the $\beta = 0$ case]; and 3) its baroclinic part $\hat{\zeta}/\tau_D$, *amplifies* those scales of the barotropic component that are most active baroclinically (see Part 1). These effects differ in their impact on flow morphology. When the drag is strong, actions 2) and 3) above cause jets to be irregular; but when drag is weak, then depending on the energy level, k_β can be small and the circulation of an azonal jet or gyre form, or k_β can be large (>3) and the jets zonal.

These processes are identifiable by their absence in drag-free circulations such as B1 and B2. These cases also illustrate the effect of *decreasing* k_β on flow character; the effect of *increasing* k_β (by altering β rather than $\tilde{U}$) is discussed in Section 5.

a. B1: k_β large, $\tau_D = \infty$

Reducing H_a^* to 0.2 and setting $\tau_D = \infty$ in the basic case A2 produces a circulation B1 that is more zonal (k_β is larger) and regular (Fig. 9). This solution displays the same characteristics as linear theory because of the enhanced importance of internal diffusion.

b. B1: k_β moderate, $\tau_D = \infty$

When the energy level of B1 is increased—by raising H_a^* to 0.5—k_β decreases to 2 (Fig. 5c) and the circulation displays ovals similar to those of the Jovian regime (Fig. 10). The large ($k_x = 2$) neutral baroclinic wave responsible for the ovals also modulates the baroclinically unstable waves, waves that have a simpler latitudinal structure than those of linear theory.

c. B2: k_β small, $\tau_D = \infty$

The high energy level ($u_1 \approx 100$ m s^{-1}) that results from setting $\tau_D = \infty$ in A2 produces a gyre form of circulation (Fig. 11). This new type of motion is consistent with a Rossby-wave instability analysis which indicates that, when k_β is small, only modes with a total wave-number less than 3 are stable—with the asymmetrical (about $y = Y/2$) modes only occurring when the angular momentum constraint is released, i.e. when $\tau_D = \infty$ (Baines, 1976). However, as in the jet mode, the baroclinic eddies still occur along the highly concentrated isotherms of the westerly flow area.

5. The rotation effect

When the rotation rate varies, changes in the Coriolis frequency f_0 alter the size (k_ρ^{-1}) and amplitude of the baroclinic eddies and their influence on the baroclinic component of the circulation; parallel changes in the Coriolis gradient β modify the value of k_β and the influence of Rossby wave propagation on the associated barotropic component. The baroclinic eddies do not affect the barotropic features directly provided they are small and weak, i.e., provided $k_\rho \gg k_\beta$ and $\hat{U} \ll \tilde{U}$. (The special situation in which the eddy scale exceeds the jet width, i.e., $k_\rho < k_\beta$, is examined in Section 6.)

To see what happens as k_β is *increased* within the jet regime, A2 is reevaluated with higher rotation rates. We are particularly interested in discovering whether multiple jets can occur in the terrestrial regime—to support our hypotheses about Jupiter's circulation—and in fact find that double jets occur when f_0 and β are increased by a factor of 4 (2 is not enough). These jets are irregular under a moderate drag ($\tau_D = 5 \times 10^5$ s) and zonal when free of drag—cases C1 and C2, respectively. For these computations, a higher longitudinal resolution is required to cope with the smaller ($L_C = 1500$ km) eddies—see Tables 1 and 2. (Although the domain size X now encompasses 16 L_C, other integrations with $X = 12 \times 10^3$ km indicate that $X = 8\ L_c$ provides solutions of similar nonlinear completeness).

a. C1: $\Omega = 4\Omega_E$, $\tau_D \neq \infty$

In statistical equilibrium, C1 exhibits two jets of 30 m s^{-1} amplitude and a temperature differential of $\Delta T \approx 85$ K (Fig. 12). The large difference between ΔT and ΔT_c indicates that this flow equilibrates at baroclinicity values far removed from

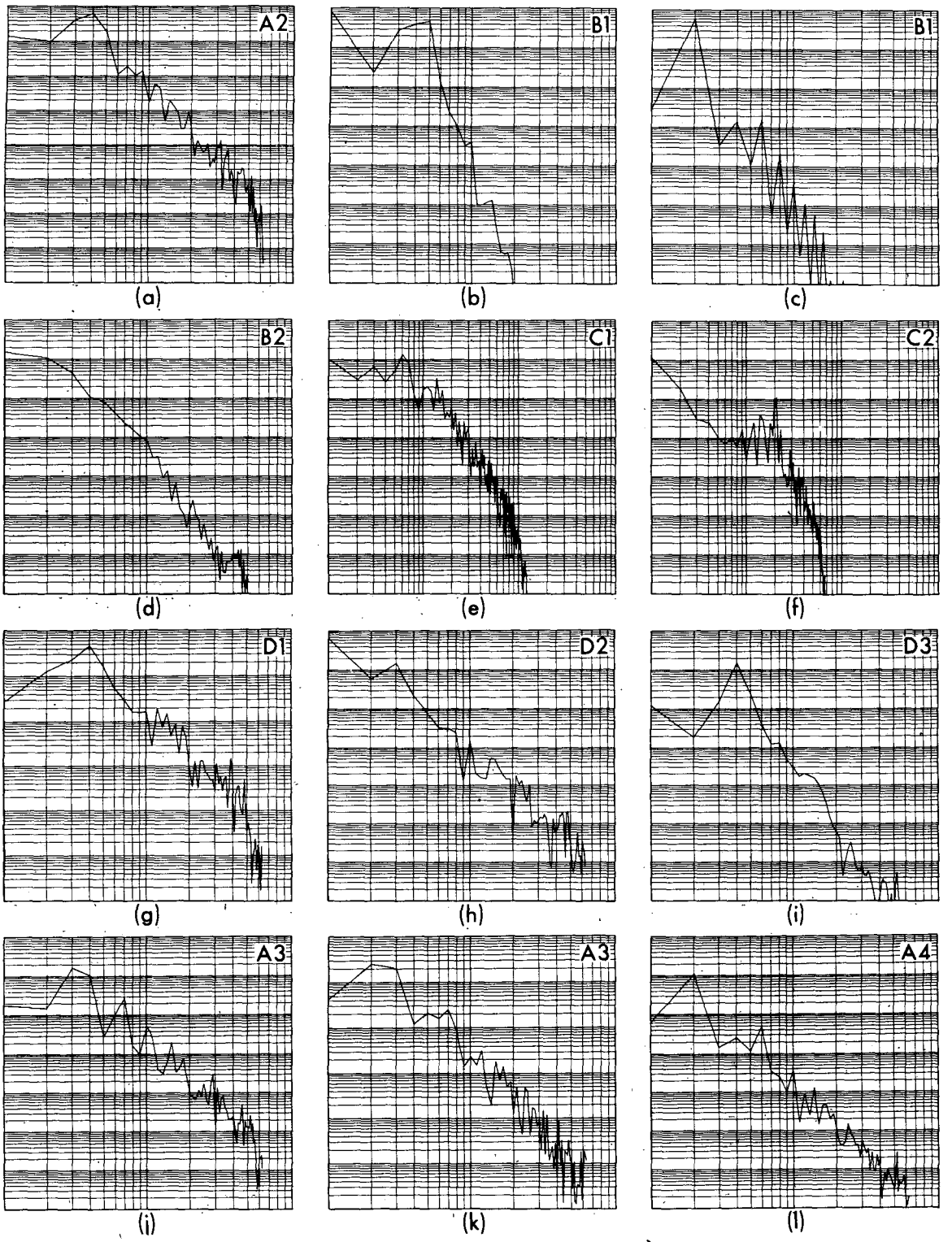

FIG. 5. Longitudinal spectra of $u^2 + v^2$ at $y' = \frac{1}{2}$, corresponding to solutions illustrated. Abscissa is wavenumber. (a) A2 at 283 days, (b) B1 at 275 days, (c) B1 at 490 days, (d) B2 at 276 days, (e) C1 at 207 days, (f) C2 at 317 days, (g) D1 at 275 days, (h) D2 at 221 days, (i) D3 at 239 days, (j) A3 at 289 days, (k) A3 at 363 days, (l) A4 at 133 days.

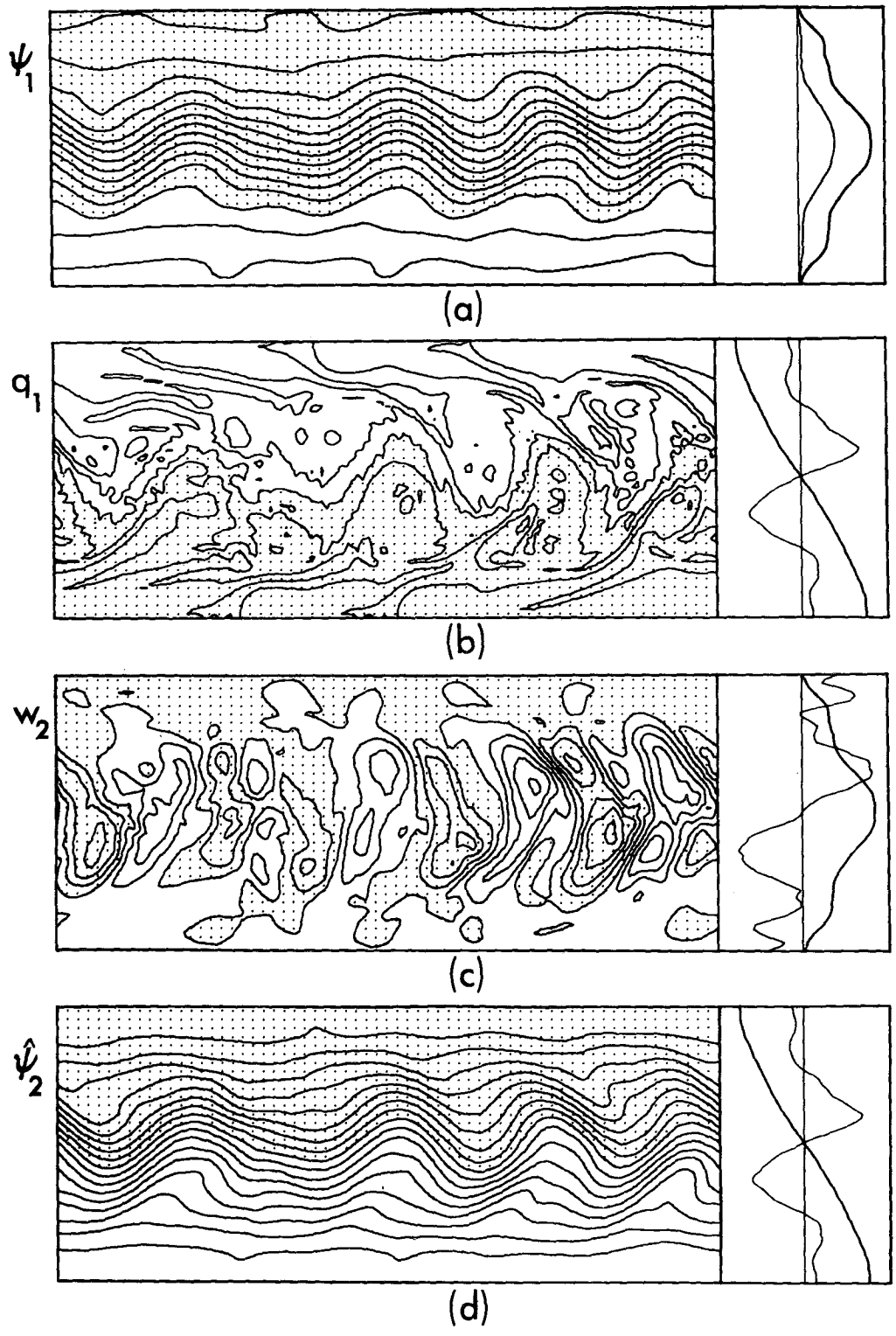

FIG. 6. Case A2 at 34 days. Notation as Fig. 1. (a) $\Delta\psi_1 = 20$ km^2 s^{-1}, $u_1^* = 60$ m s^{-1}, $u_3^* = 60$ m s^{-1}; (b) $\Delta q_1 = 6 \times 10^{-5}$ s^{-1}, $T_2^* = 40$ K, $w_2^* = 10^{-5}$ km s^{-1}; (c) $\Delta w_2 = 1.5 \times 10^{-5}$ km s^{-1}, $u_1^* = 60$ m s^{-1}, $\zeta_2^* = 2 \times 10^{-5}$ s^{-1}, (d) $\Delta\hat{\psi}_2 = 10$ km^2 s^{-1}, $T_2^* = 40$ K, $w_2^* = 10^{-5}$ km s^{-1}.

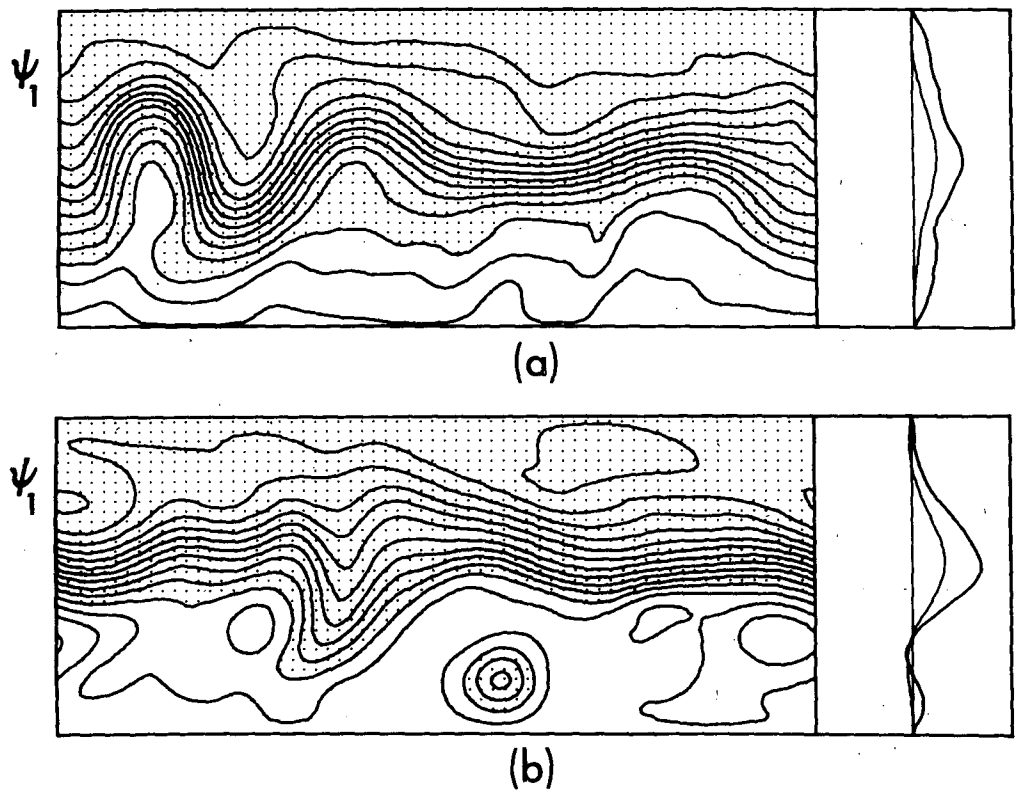

FIG. 7. Case A2 at (a) 41 days, (b) 48 days. $\Delta\psi_1 = 20$ km s^{-1}, $u_1^* = 100$ m s^{-1}, $u_3^* = 100$ m s^{-1}.

TABLE 4. Case A2. Instantaneous global means of energy and energy conversion rates. Units are 10^{-6} km^2 s^{-2} for K', $\bar{K}$, P'; 10^{-5} km^2 s^{-2} for $\bar{P}$; 10^{-12} km^2 s^{-3} for conversion terms; m s^{-1} for U_1, U_3 and K for ΔT. Time measured from end of axisymmetric spinup.

Days	ΔT	$-2\dot{\psi}_L$	U_1	U_3	K'	$\bar{K}$	P'	$\bar{P}$	$\{Q\bar{P}\}$	$\{\bar{P}P'\}$	$\{P'K'\}$	$\{K'\bar{K}\}$	$\{\bar{P}\bar{K}\}$	$\{\bar{K}D\}$	$\{\bar{K}'D\}$	$\{\bar{K}F\}$	$\{K'F\}$	$\{\bar{P}F\}$	$\{P'F\}$
0	52.7	291	23.5	7.3	0	301	0	194	439	0	0	0	40	−24	0	4	0	20	0
17.3	60.3	335	27.0	8.5	0	399	0	254	503	4	3	1	46	−28	0	5	0	26	0
34.5	60.1	354	34.6	19.4	165	535	65	262	510	1425	1152	538	−128	219	115	10	53	26	11
48.3	47.9	309	40.2	22.8	301	670	122	198	431	508	673	1099	−369	438	131	27	93	25	18
62.1	43.0	263	39.9	29.1	573	374	237	157	390	411	695	595	−153	174	323	9	105	16	28
75.9	40.0	240	36.5	25.1	413	374	159	148	375	613	507	−299	−47	145	239	12	79	17	20
89.7	41.2	238	35.5	24.6	400	333	197	147	377	919	630	256	−145	128	138	9	74	16	22
103.5	40.5	236	34.7	23.9	374	334	157	144	373	83	242	82	−59	132	173	10	75	15	19
117.3	39.6	231	33.6	21.8	305	354	132	147	376	630	758	945	−234	154	113	11	62	16	18
131.1	37.1	224	36.1	25.7	465	300	164	118	338	269	388	214	−112	145	173	9	97	13	25
144.9	36.3	214	32.8	21.5	301	329	120	126	346	636	490	223	−140	169	93	10	68	14	18
158.7	36.1	211	31.4	18.6	215	368	68	125	341	426	300	270	−130	163	122	18	58	16	11
172.5	39.0	222	30.2	19.3	246	283	94	131	354	304	234	−30	−35	65	114	10	51	15	12
186.3	39.7	229	31.7	21.4	308	279	115	131	357	387	293	44	−55	98	152	7	68	13	15
200.1	41.3	236	30.5	18.0	208	331	82	148	377	448	280	−119	−43	104	89	10	49	16	11
213.9	41.3	240	33.2	22.4	312	333	125	138	366	471	640	873	−182	166	121	10	69	15	18
227.7	40.5	235	32.9	22.5	334	302	122	139	367	421	406	98	−71	97	192	8	70	15	17
241.5	40.2	234	33.8	23.0	354	317	131	138	365	308	534	578	−125	129	205	8	75	15	19
255.3	39.6	227	32.4	20.1	240	385	73	139	363	310	307	−454	−18	182	170	19	60	17	12
282.9	39.7	230	31.9	20.9	269	324	108	142	369	429	506	364	−101	108	117	9	55	16	15

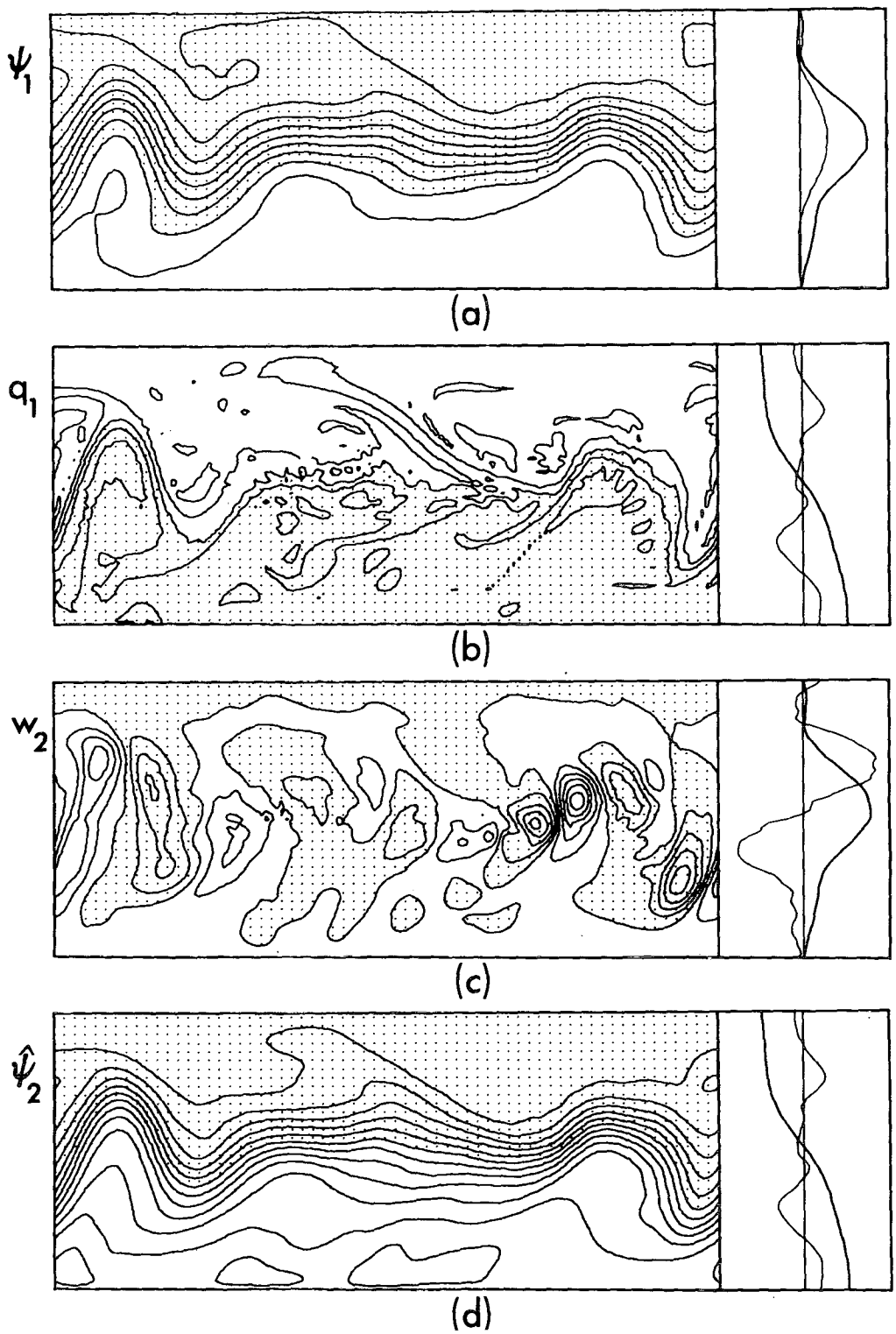

FIG. 8. Case A2 at 283 days. Notation as Fig. 2. Contour values as Fig. 6.

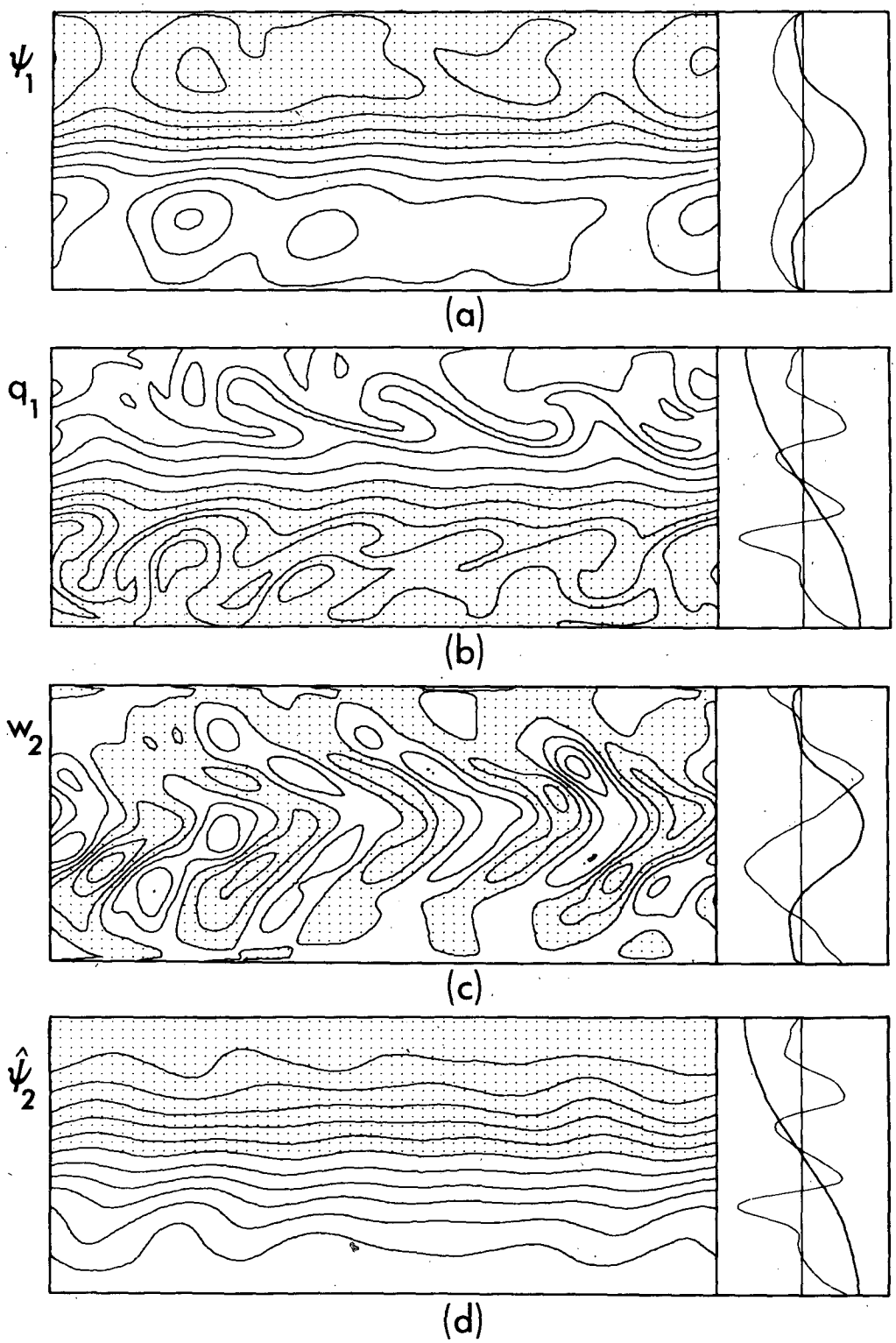

FIG. 9. Case B1 at 275 days. Notation as Fig. 1. (a) $\Delta\psi_1 = 10$ km^2 s^{-1}, $u_1^* = 30$ m s^{-1}, $u_3^* = 30$ m s^{-1}; (b) $\Delta q_1 = 2 \times 10^{-5}$ s^{-1}, $T_2^* = 30$ K, $w_2^* = 5 \times 10^{-7}$ km s^{-1}; (c) $\Delta w_2 = 3 \times 10^{-6}$ km s^{-1}, $u_1^* = 30$ m s^{-1}, $\zeta_2^* = 1.5 \times 10^{-5}$ s^{-1}; (d) $\Delta\hat{\psi}_2 = 10$ km^2 s^{-1}, $T_2^* = 30$ K, $w_2^* = 5 \times 10^{-7}$ km s^{-1}.

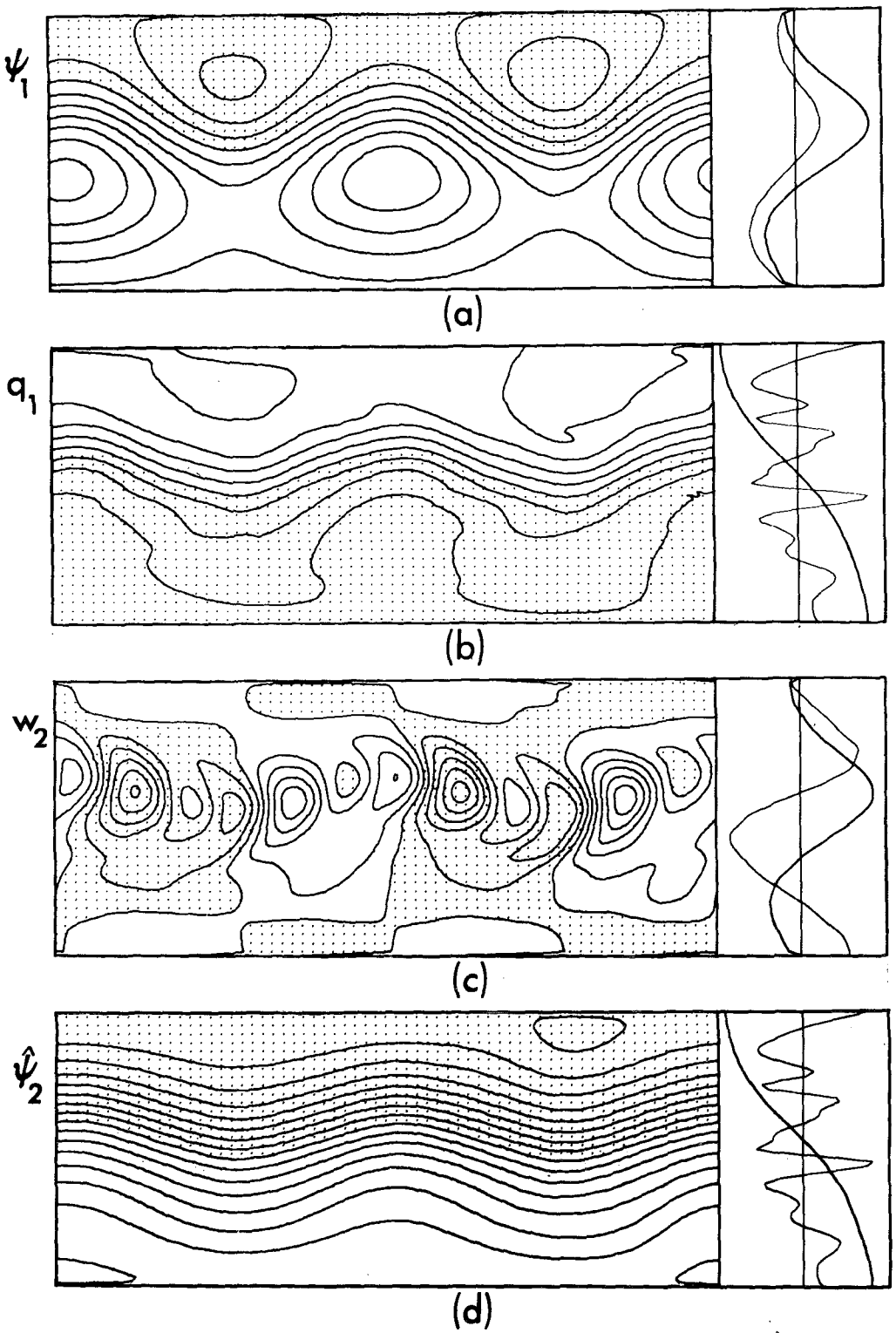

FIG. 10. Case B1 at 490 days. Notation as Fig. 1. (a) $\Delta\psi_1 = 20$ km^2 s^{-1}, $u_1^* = 50$ m s^{-1}, $u_3^* = 50$ m s^{-1}; (b) $\Delta q_1 = 3 \times 10^{-5}$ s^{-1}, $T_2^* = 30$ K, $w_2^* = 2 \times 10^{-7}$ km s^{-1}; (c) $\Delta w_2 = 2.5 \times 10^{-6}$ km s^{-1}, $u_1^* = 50$ m s^{-1}, $\zeta_2^* = 2.5 \times 10^{-5}$ s^{-1}; (d) $\Delta\hat{\psi}_2 = 10$ km^2 s^{-1}, $T_2^* = 30$ K, $w_2^* = 2 \times 10^{-7}$ km s^{-1}.

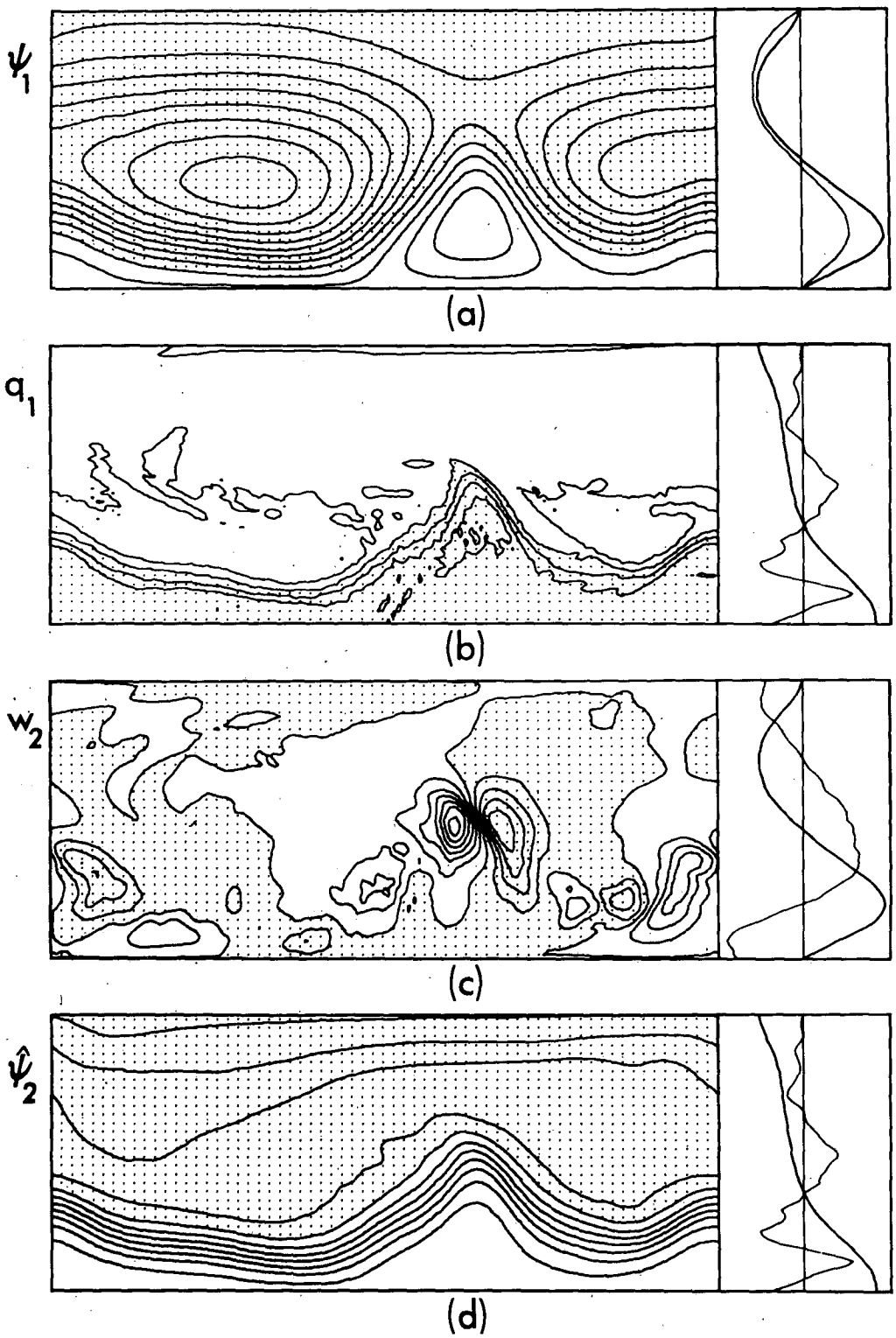

FIG. 11. Case B2 at 276 days. Notation as Fig. 1. (a) $\Delta\psi_1 = 40$ km^2 s^{-1}, $u_1^* = 100$ m s^{-1}, $u_3^* = 100$ m s^{-1}; (b) $\Delta q_1 = 8 \times 10^{-5}$ s^{-1}, $T_2^* = 40$ K, $w_2^* = 5 \times 10^{-6}$ km s^{-1}; (c) $\Delta w_2 = 2 \times 10^{-5}$ km s^{-1}, $u_1^* = 100$ m s^{-1}, $\zeta_2^* = 6 \times 10^{-5}$ s^{-1}; (d) $\Delta\hat{\psi}_2 = 15$ km^2 s^{-1}, $T_2^* = 40$ K, $w_2^* = 5 \times 10^{-6}$ km s^{-1}.

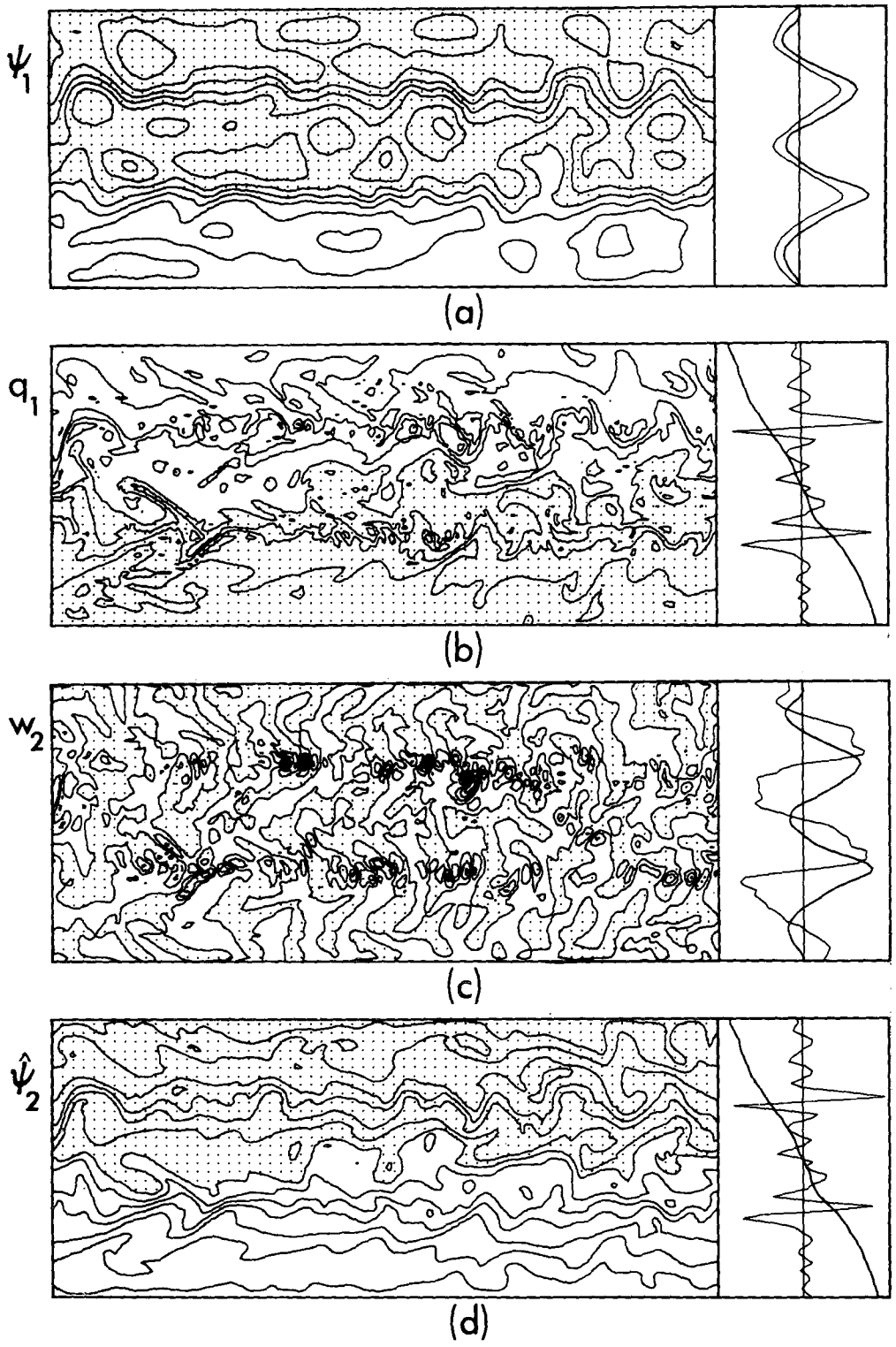

FIG. 12. Case C1 at 207 days. Notation as Fig. 1. (a) $\Delta\psi_1 = 10$ km^2 s^{-1}, $u_1^* = 40$ m s^{-1}, $u_3^* = 40$ m s^{-1}; (b) $\Delta q_1 = 2 \times 10^{-4}$ s^{-1}, $T_2^* = 50$ K, $w_2^* = 5 \times 10^{-6}$ km s^{-1}; (c) $\Delta w_2 = 3 \times 10^{-5}$ km s^{-1}, $u_1^* = 40$ m s^{-1}, $\zeta_2^* = 4 \times 10^{-5}$ s^{-1}; (d) $\Delta\hat{\psi}_2 = 5$ km^2 s^{-1}, $T_2^* = 50$ K, $w_2^* = 5 \times 10^{-6}$ km s^{-1}.

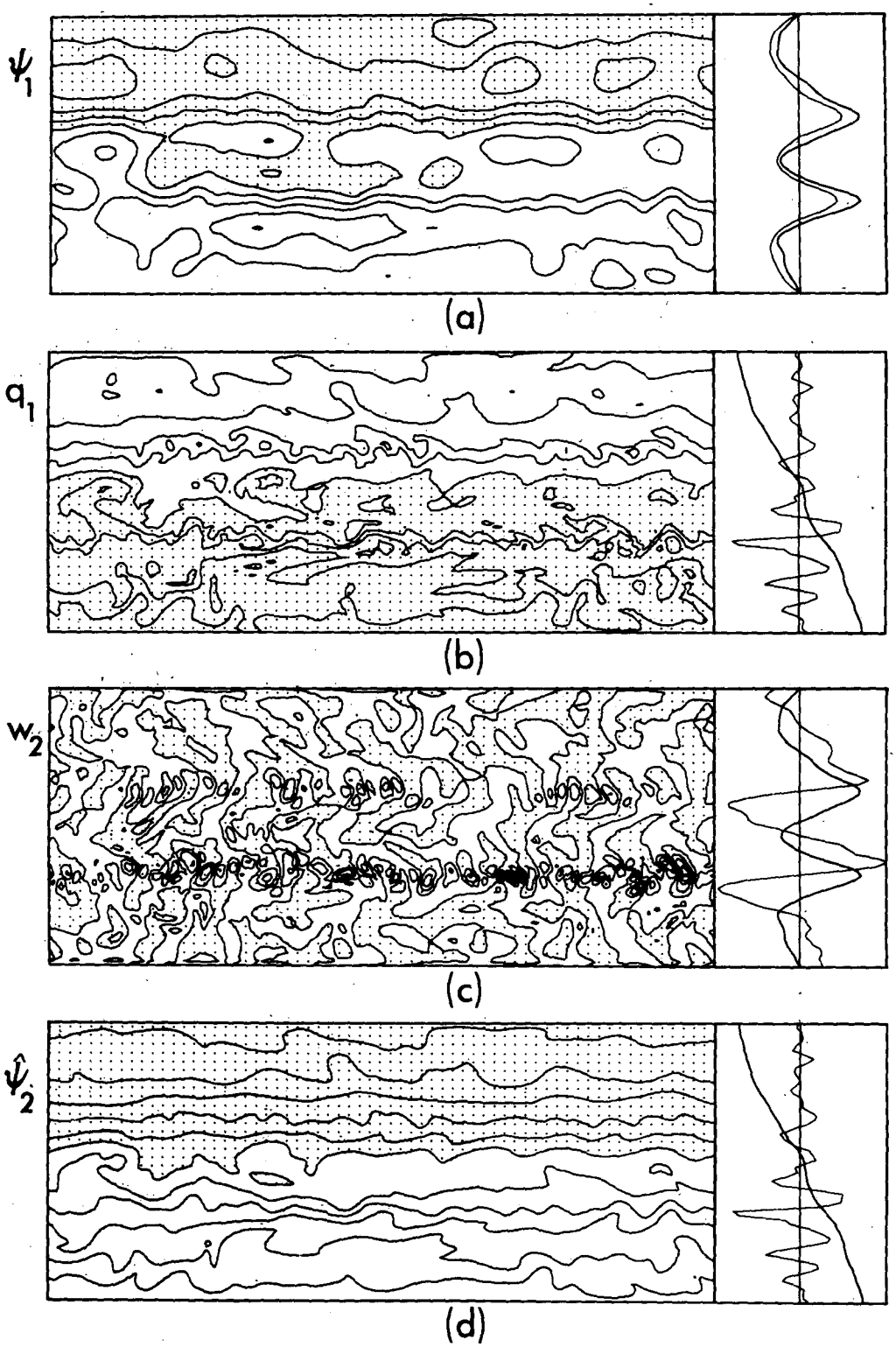

FIG. 13. Case C2 at 138 days. Notation as Fig. 1. (a) $\Delta\psi_1 = 10$ km^2 s^{-1}, $u_1^* = 40$ m s^{-1}, $u_3^* = 40$ m s^{-1}; (b) $\Delta q_1 = 1.5 \times 10^{-4}$ s^{-1}, $T_2^* = 50$ K, $w_2^* = 1.5 \times 10^{-6}$ km s^{-1}; (c) $\Delta w_2 = 1 \times 10^{-5}$ km s^{-1}, $u_1^* = 40$ m s^{-1}, $\zeta_2^* = 4 \times 10^{-5}$ s^{-1}; (d) $\Delta\hat{\psi}_2 = 5$ km s^{-1}, $T_2^* = 50$ K, $w_2^* = 1.5 \times 10^{-6}$ km s^{-1}.

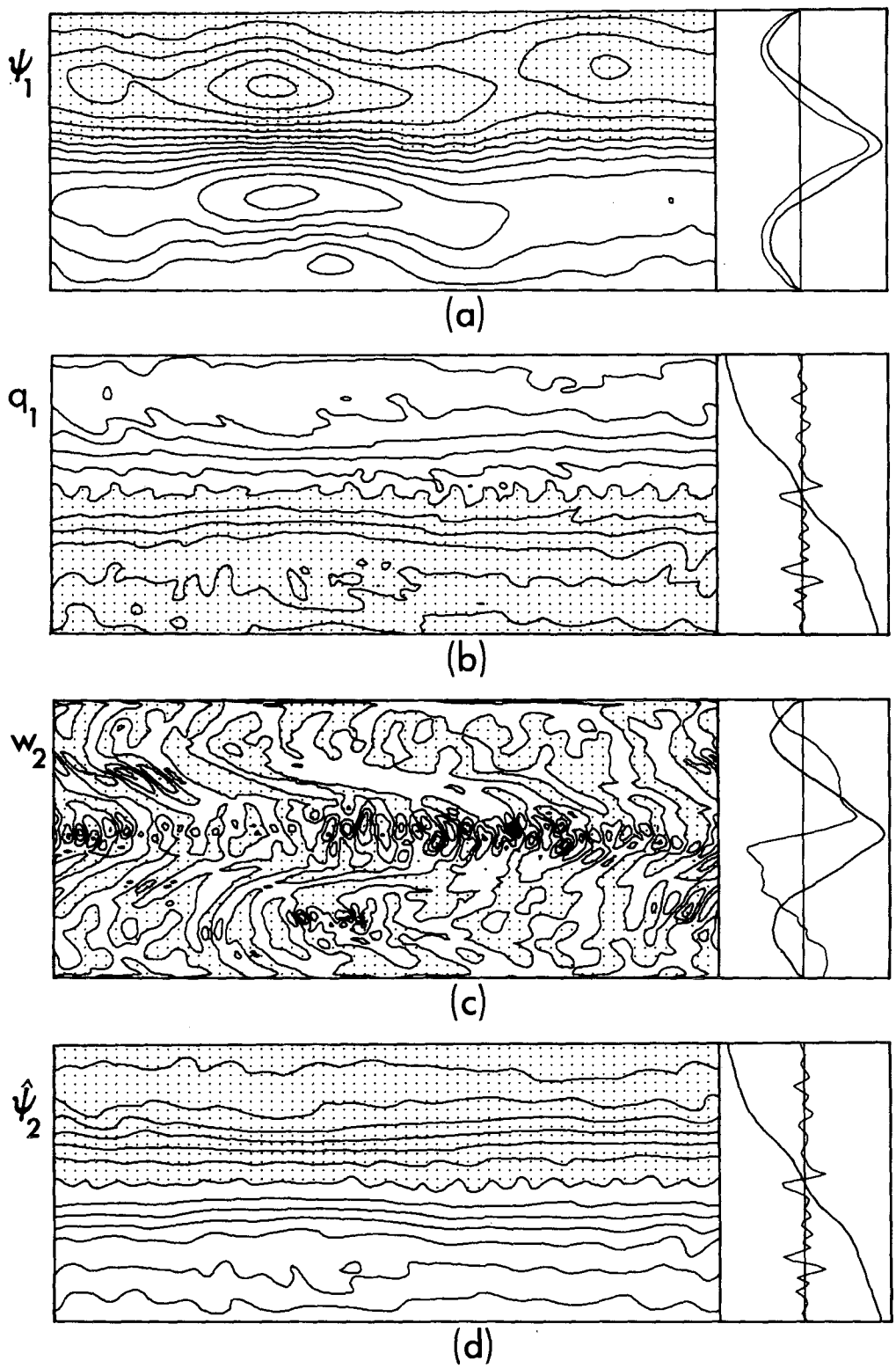

FIG. 14. Case C2 at 317 days. Notation as Fig. 1. Contour intervals as Fig. 13 but with $\Delta w = 5 \times 10^{-6}$ km s^{-1} in (c).

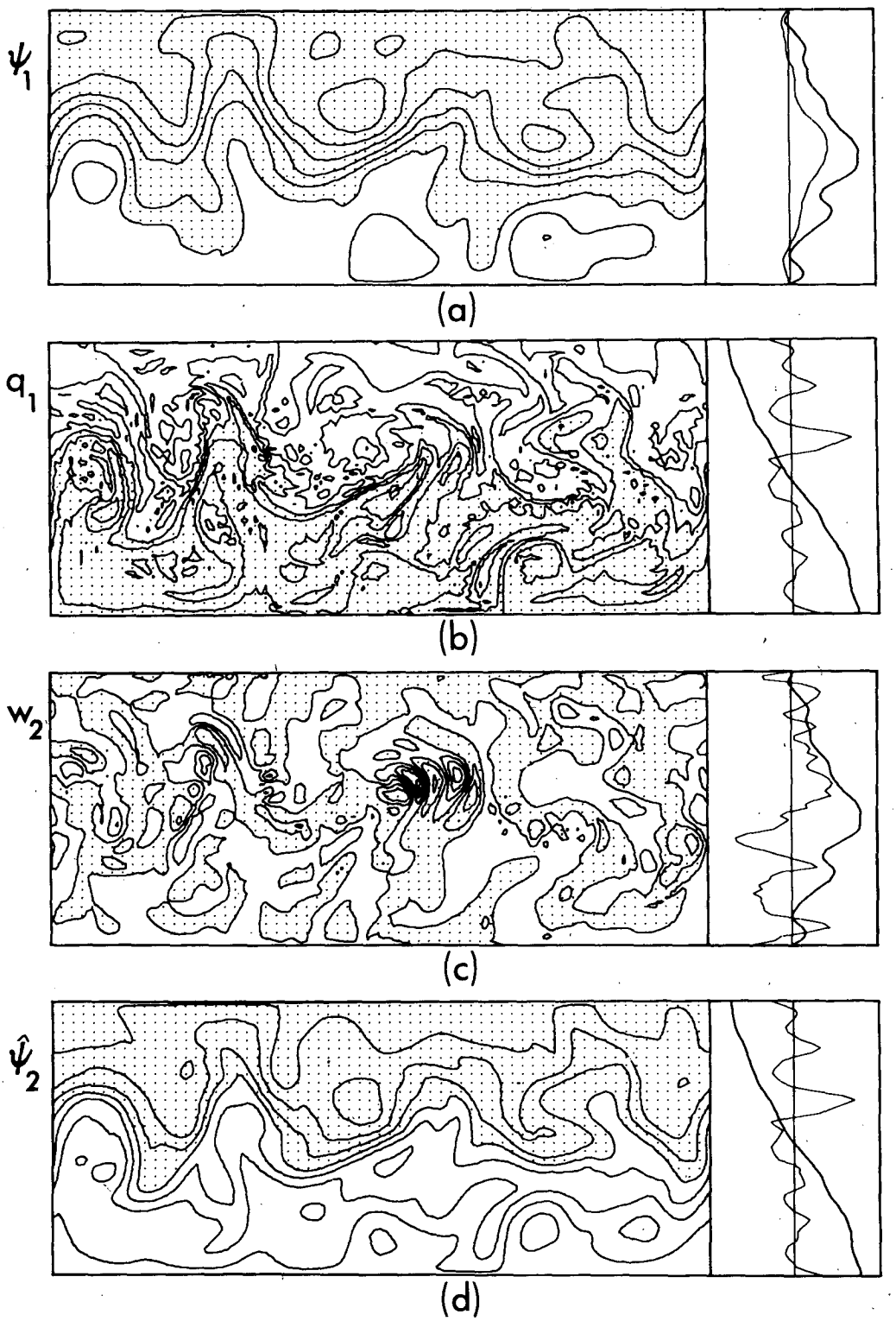

FIG. 15. Case D1 at 275 days. Notation as Fig. 1. (a) $\Delta\psi_1 = 20$ km^2 s^{-1}, $u_1^* = 30$ m s^{-1}, $u_3^* = 30$ m s^{-1}; (b) $\Delta q_1 = 1 \times 10^{-4}$ s^{-1}, $T_2^* = 15$ K, $w_2^* = 2 \times 10^{-5}$ km s^{-1}; (c) $\Delta w_2 = 5 \times 10^{-5}$ km s^{-1}, $u_1^* = 30$ m s^{-1}, $\zeta_2^* = 2 \times 10^{-5}$ s^{-1}; (d) $\Delta\hat{\psi}_2 = 10$ km^2 s^{-1}, $T_2^* = 15$ K, $w_2^* = 2 \times 10^{-5}$ km s^{-1}.

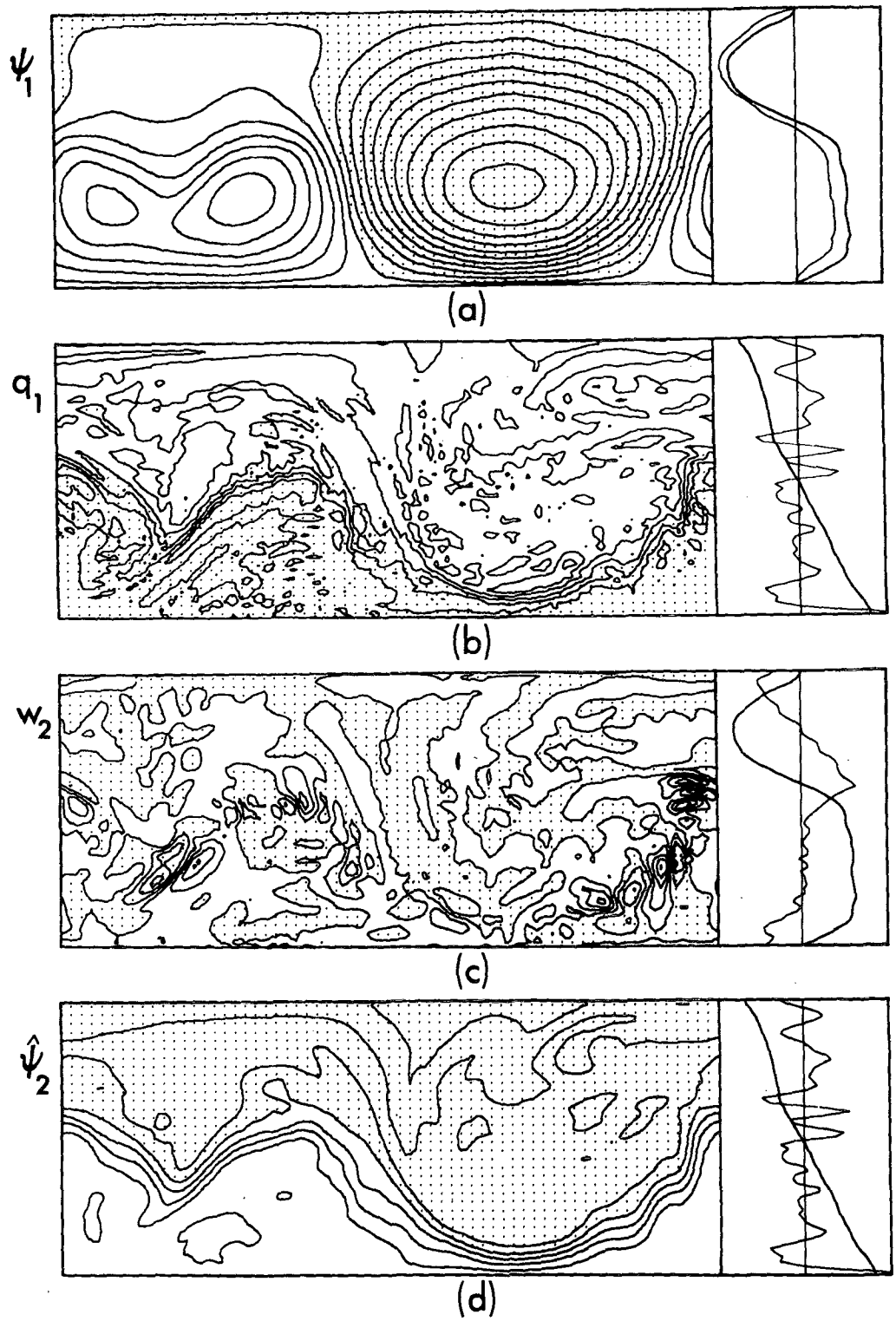

FIG. 16. Case D2 at 221 days. Notation as Fig. 1. (a) $\Delta\psi_1 = 40$ km^2 s^{-1}, $u_1^* = 40$ m s^{-1}, $u_3^* = 40$ m s^{-1}; (b) $\Delta q_1 = 1 \times 10^{-4}$ s^{-1}, $T_2^* = 15$ K, $w_2^* = 1.5 \times 10^{-5}$ km s^{-1}; (c) $\Delta w_2 = 5 \times 10^{-5}$ km s^{-1}, $u_1^* = 40$ m s^{-1}, $\zeta_2^* = 5 \times 10^{-5}$ s^{-1}; (d) $\Delta\hat{\psi}_2 = 10$ km^2 s^{-1}, $T_2^* = 15$ K, $w_2^* = 1.5 \times 10^{-5}$ km s^{-1}.

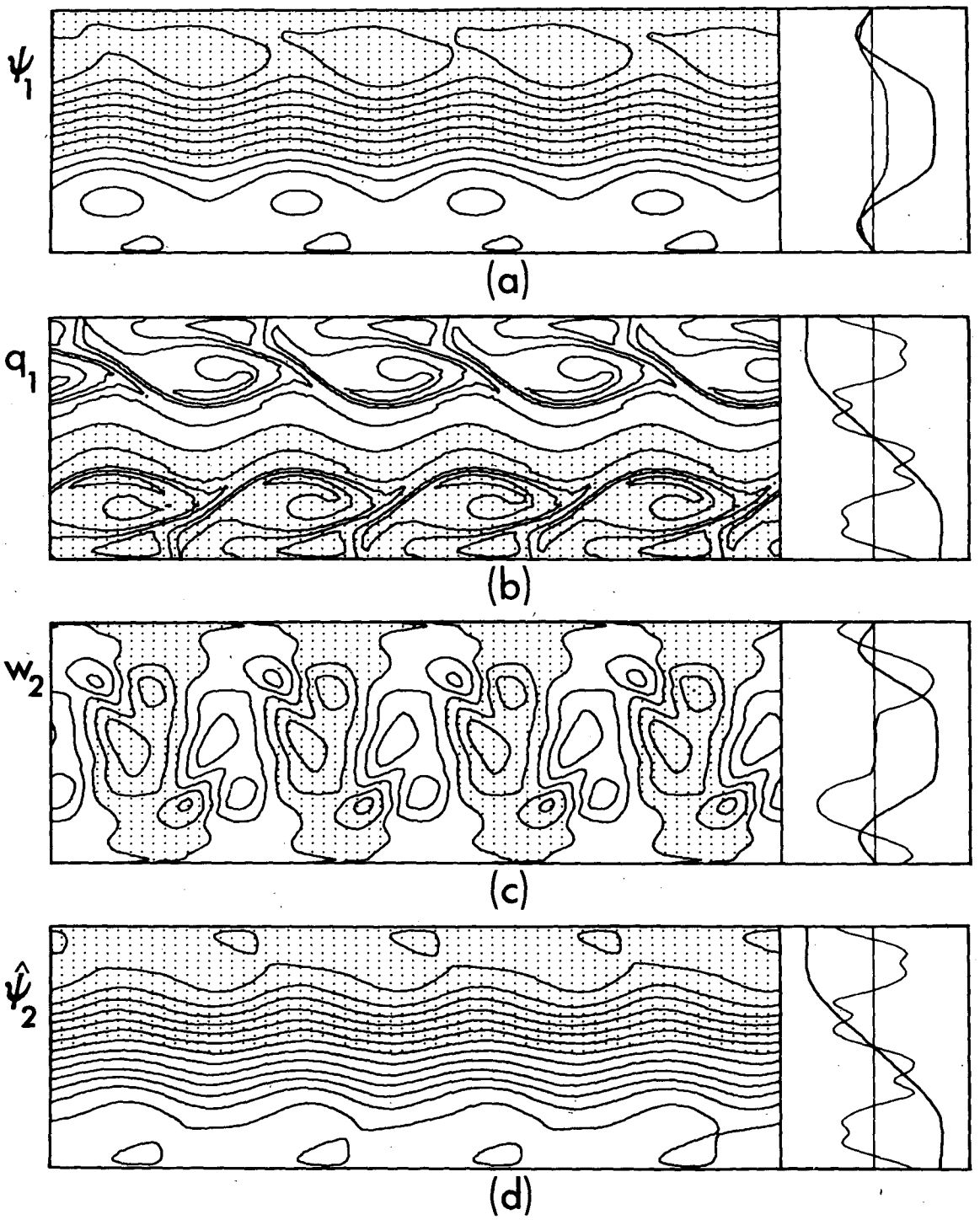

FIG. 17. Case D3 at 46 days. Notation as Fig. 1. (a) $\Delta\psi_1 = 30\,\text{km}^2\,\text{s}^{-1}, u_1^* = 100\,\text{m s}^{-1}, u_3^* = 100\,\text{m s}^{-1}$; (b) $\Delta q_1 = 3 \times 10^{-5}$ s^{-1}, $T_2^* = 60$ K, $w_2^* = 1.5 \times 10^{-6}$ km s^{-1}; (c) $\Delta w_2 = 7 \times 10^{-6}$ km s^{-1}, $u_1^* = 100$ m s^{-1}, $\zeta_2^* = 5 \times 10^{-5}$ s^{-1}; (d) $\Delta\hat{\psi}_2 = 20$ $\text{km}^2\,\text{s}^{-1}$, $T_2^* = 60$ K, $w_2^* = 1.5 \times 10^{-6}$ km s^{-1}.

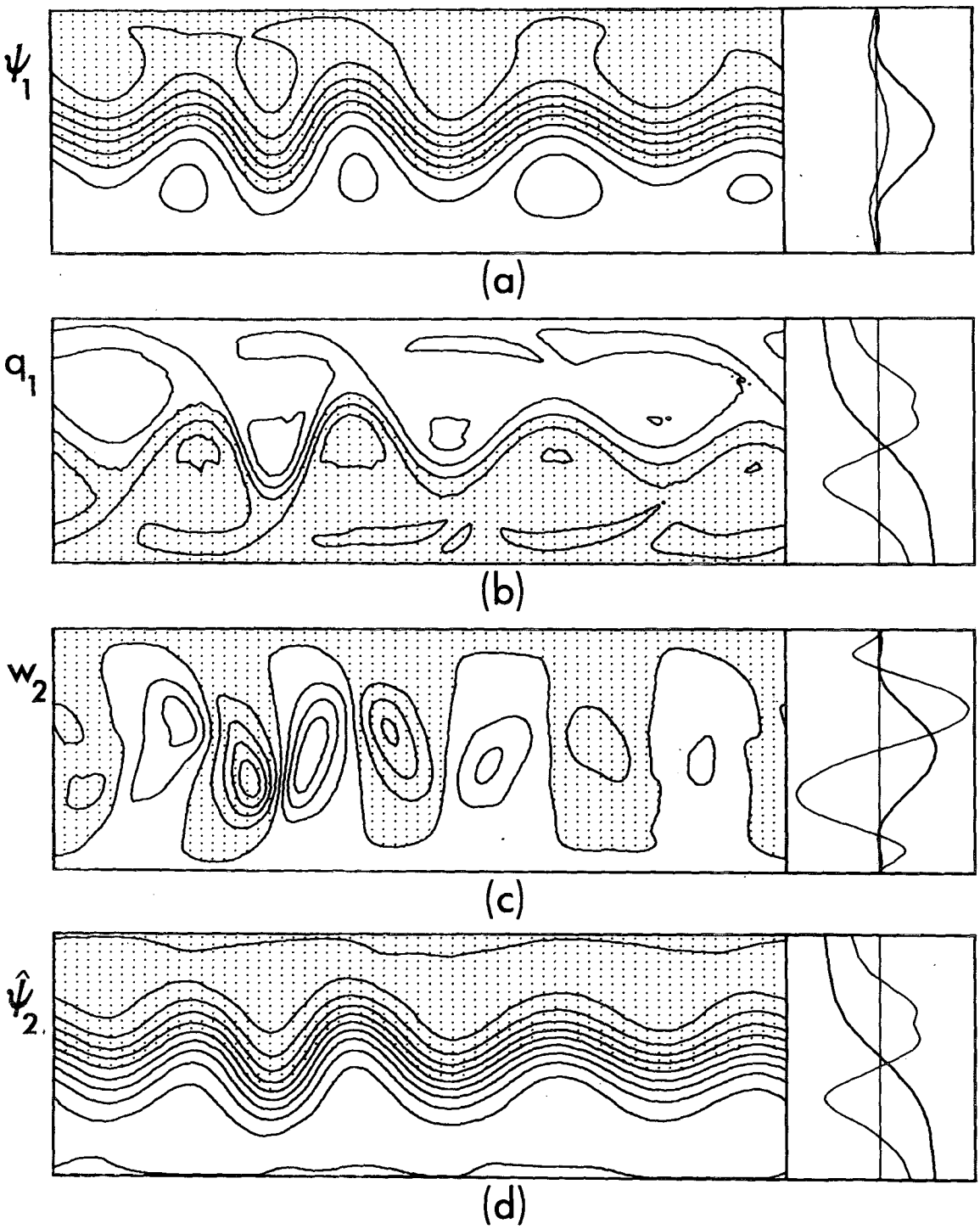

FIG. 18. Case D3 at 239 days. Notation as Fig. 1, (a) $\Delta\psi_1 = 30\,\text{km}^2\,\text{s}^{-1}, u_1^* = 100\,\text{m s}^{-1}, u_3^* = 100\,\text{m s}^{-1}$; (b) $\Delta q_1 = 5 \times 10^{-5}$ s^{-1}, $T_2^* = 60$ K, $w_2^* = 1.5 \times 10^{-6}$ km s^{-1}; (c) $\Delta w_2 = 1.2 \times 10^{-5}$ km s^{-1}, $u_1^* = 100$ m s^{-1}, $\zeta_2^* = 2 \times 10^{-5}\,\text{s}^{-1}$; (d) $\Delta\hat{\psi}_2 = 20$ $\text{km}^2\,\text{s}^{-1}$, $T_2^* = 60$ K, $w_2^* = 1.5 \times 10^{-6}$ km s^{-1}.

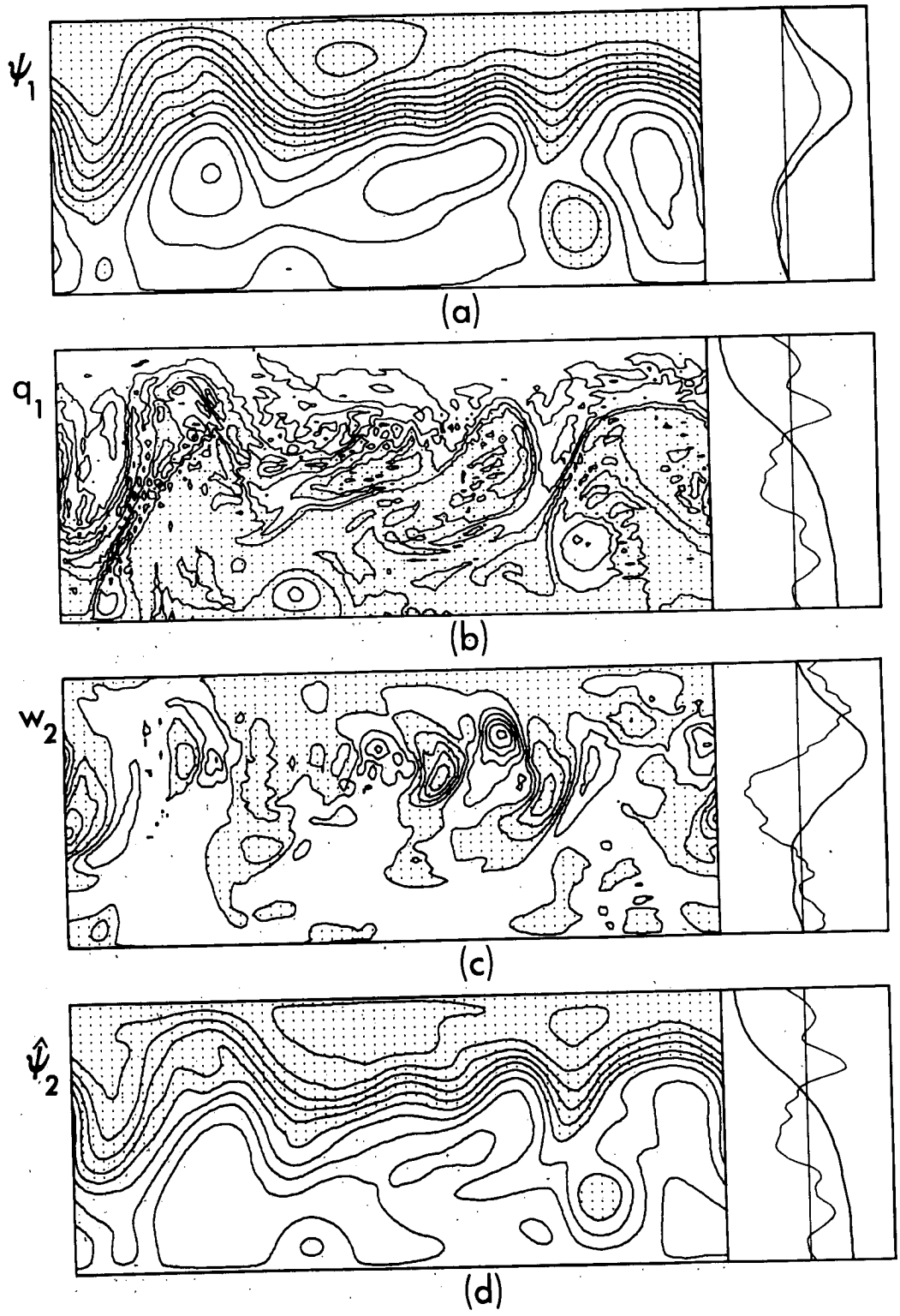

FIG. 19. Case A3 at 289 days. Notation as Fig. 1. (a) $\Delta\psi_1 = 30\ \text{km}^2\ \text{s}^{-1}$, $u_1^* = 100\ \text{m s}^{-1}$, $u_3^* = 100\ \text{m s}^{-1}$; (b) $\Delta q_1 = 1 \times 10^{-4}\ \text{s}^{-1}$, $T_2^* = 40$ K, $w_2^* = 3 \times 10^{-5}\ \text{km s}^{-1}$; (c) $\Delta w_2 = 5 \times 10^{-5}\ \text{km s}^{-1}$, $u_1^* = 100\ \text{km s}^{-1}$, $\zeta_2^* = 5 \times 10^{-5}\ \text{s}^{-1}$; (d) $\Delta\hat{\psi}_2 = 20\ \text{km}^2\ \text{s}^{-1}$, $T_2^* = 40$ K, $w_2^* = 3 \times 10^{-5}\ \text{km s}^{-1}$.

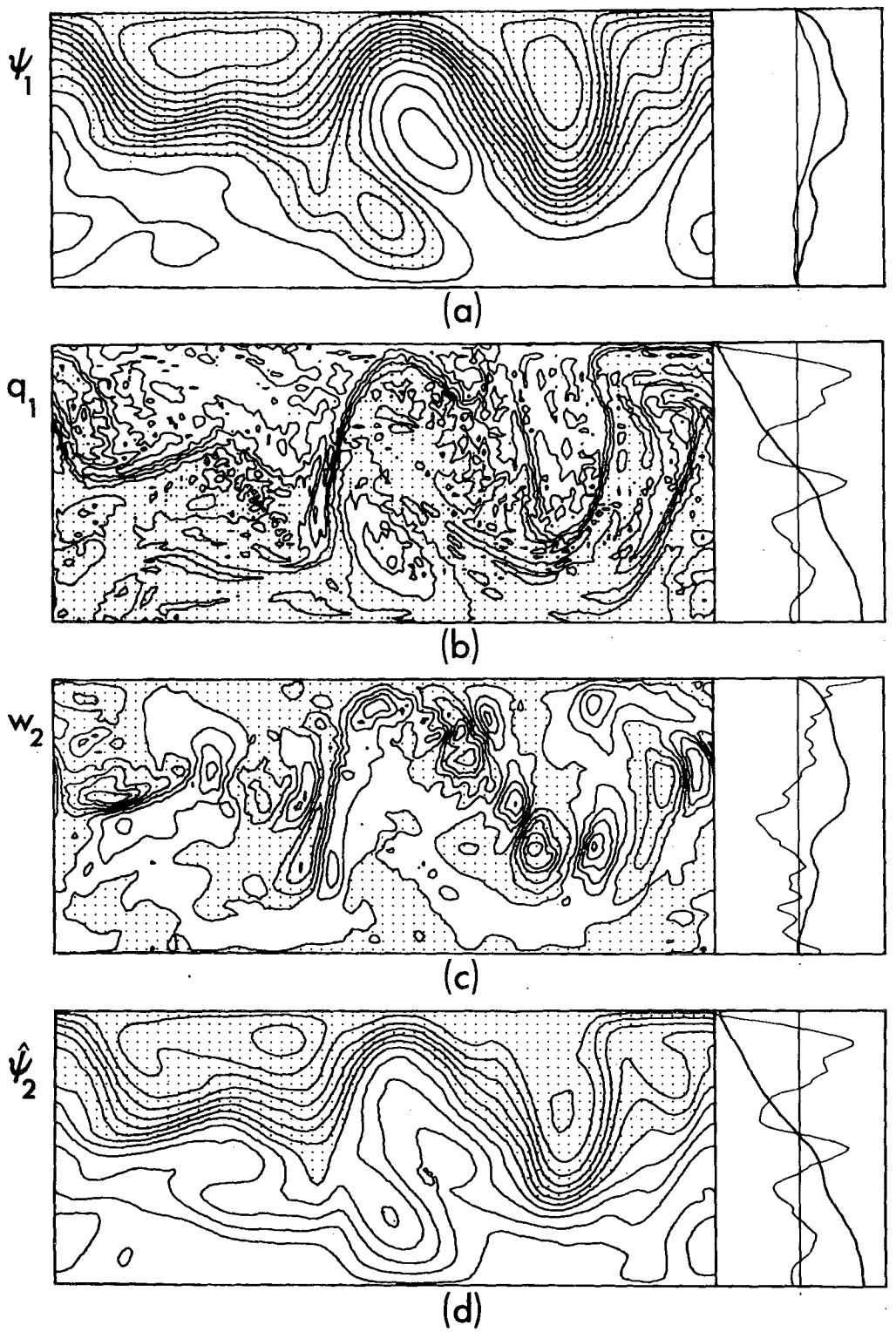

FIG. 20. Case A3 at 353 days. Notation as Fig. 1. (a) $\Delta\psi_1 = 30$ km^2 s^{-1}, $u_1^* = 100$ m s^{-1}, $u_3^* = 100$ m s^{-1}; (b) $\Delta q_1 = 1 \times 10^{-4}$ s^{-1}, $T_2^* = 40$ K, $w_2^* = 3 \times 10^{-5}$ km s^{-1}; (c) $\Delta w_2 = 5 \times 10^{-5}$ km s^{-1}, $u_1^* = 100$ m s^{-1}, $\zeta_2^* = 5 \times 10^{-5}$ s^{-1}; (d) $\Delta\hat{\psi}_2 = 20$ km^2 s^{-1}, $T_2^* = 40$ K, $w_2^* = 3 \times 10^{-5}$ km s^{-1}.

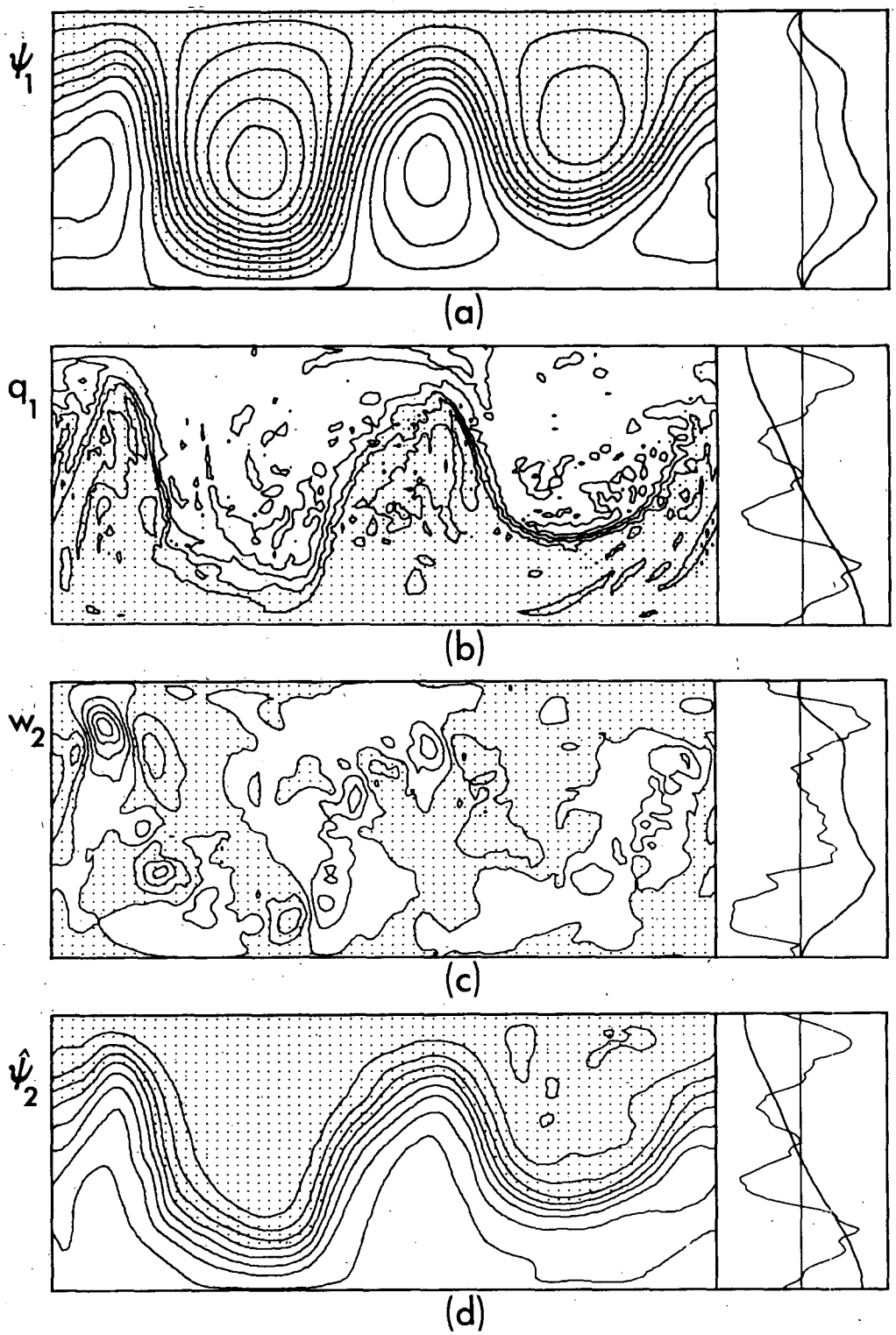

FIG. 21. Case A4 at 133 days. Notation as Fig. 1. (a) $\Delta\psi_1 = 40$ km^2 s^{-1}, $u_1^* = 50$ m s^{-1}, $u_3^* = 50$ m s^{-1}; (b) $\Delta q_1 = 1 \times 10^{-4}$ s^{-1}, $T_2^* = 40$ K, $w_2^* = 1 \times 10^{-5}$ km s^{-1}; (c) $\Delta w_2 = 5 \times 10^{-5}$ km s^{-1}, $u_1^* = 50$ m s^{-1}, $\zeta_2^* = 2 \times 10^{-5}$ s^{-1}; (d) $\Delta\hat{\psi}_2 = 20$ km^2 s^{-1}, $T_2^* = 40$ K, $w_2^* = 1 \times 10^{-5}$ km s^{-1}.

TABLE 5. Final values of instantaneous global means of energy and energy conversion rates of all cases presented. Units are 10^{-6} km^2 s^{-2} for K', $\bar{K}$, P'; 10^{-5} km^2 s^{-2} for $\bar{P}$; 10^{-12} km^2 s^{-3} for conversion terms. Time measured from end of axisymmetric spinup.

Case	Days	K'	$\bar{K}$	P'	$\bar{P}$	$\{Q\bar{P}\}$	$\{\bar{P}P'\}$	$\{P'K'\}$	$\{K'\bar{K}\}$	$\{\bar{P}\bar{K}\}$	$\{\bar{K}D\}$	$\{K'D\}$	$\{\bar{K}F\}$	$\{K'F\}$	$\{\bar{P}F\}$	$\{P'F\}$
A1	412.2	267	286	122	132	358	577	486	260	−75	96	44	47	117	42	46
A2	282.9	269	324	108	142	369	429	506	364	−101	108	117	9	55	16	15
A3	352.7	2672	718	1011	301	4352	2839	3554	−866	34	414	3014	21	433	35	96
A4	133.4	4548	390	1196	200	1785	1353	1266	−1833	184	17	1071	9	314	21	67
B1	490.3	185	349	53	213	228	−2	5	0	9	—	—	33	17	44	4
B2	316.9	2365	1704	344	171	401	920	524	822	24	—	—	73	138	27	23
C1	206.9	152	146	79	461	677	734	518	140	−13	105	45	32	238	53	92
C2	317.3	49	271	14	578	377	24	33	44	1	—	—	23	23	63	8
D1	275.4	326	100	236	148	764	1114	718	34	−10	82	358	5	160	16	62
D2	220.7	5379	440	635	103	636	362	371	−1114	−7	—	—	23	258	14	56
D3	239.2	332	470	97	165	240	307	294	173	−94	45	50	30	75	36	18

the neutral instability curve; this, plus the absence of organized meridional circulations, suggests that a circulation with smaller eddies is more nonlinear. Otherwise the two jets resemble repetitions of the terrestrial jet.

Baroclinic eddy activity is longitudinally localized within the maximum westerly flow areas, with longitudinal and latitudinal scales equal to the radius of deformation (Fig. 12c). The spectral peaks in Fig. 5e correspond to $k_\beta = 6$ and $k_\rho = 16$.

b. C2: $\Omega = 4\Omega_E$, $\tau_D = \infty$

In the absence of drag the circulation C2 initially develops in the same way as C1 except that the jets are more regular (Fig. 13), until 190 days when the two 30 m s^{-1} jets coalesce into a single, wider, more regular jet that equilibrates with an amplitude of 40 m s^{-1} (Fig. 14). This merger occurs because of the ineffectiveness of the internal dissipation in curbing the growth of the energy level and the inability of the domain to accommodate two jets of width L_β when $\bar{U} > 20$ m s^{-1}.

6. The static stability effect

Changes in the static stability alter the baroclinic eddy size and structure in the same way as changes in the rotation rate, but, unlike the latter, they have no parallel effect on the barotropic component.

a. D1: $s = 1/4$, $\tau_D \neq \infty$

When the static stability of A2 is decreased to the extent that eddies are half their normal size ($k_\rho = 8$), the amplification of the smaller baroclinic scales by the drag increases the irregularity of the circulation (Fig. 15). Flow morphology resembles that of other small-eddy cases (e.g., C1).

b. D2: $s = 1/4$, $\tau_D = \infty$

If the surface drag is removed from D1, the fluid displays the characteristics of a high energy level, drag-free flow (e.g., B2) in which gyres prevail and baroclinic details lose their significance, i.e. $k_\beta < 1$ and $k_\rho \gg k_\beta$ (Fig. 16). Similar domain-sized modes also occur in studies of the barotropic response of the Venus stratosphere (Rossow and Williams, 1979, Fig. 2). In all these cases, a mode that is odd about the center of the domain ($y = Y/2$) arises due to the relaxation of the angular momentum constraint (Baines, 1976).

c. D3: $s = 3$, $\tau_D \neq \infty$

Increasing the static stability of A2 to produce eddies with a longitudinal scale equal to Y fails to yield the theoretically expected $k_\rho = 3$ wave (even though $X = 3Y$, Table 2); instead a $k_x = 4$ mode evolves as in Fig. 5i. Releasing potential energy at this relatively small wavenumber ($k_\rho \approx k_\beta$) leads to regular flow both at the beginning and at the end of the calculation (Figs. 17 and 18). The predominance of this mode is reflected in the clearly structured cyclogenesis, albeit localized in x, and the triple-cell circulation (Fig. 18).

In the above solutions, the mean baroclinicity ΔT exceeds or falls short of the critical value ΔT_c (given by Phillips' theory) depending upon whether the eddies are smaller or larger than those in A2 (cf. Tables 1 and 2). We conclude therefore that the result that $\Delta T \approx \Delta T_c$ for the existing circulation is mainly coincidental.

7. Stability of the basic circulation

Given that quasi-geostrophic circulations are sensitive to parameter changes, we now examine the *stability* of the present terrestrial configuration (as

represented by the A2 solution). We are particularly interested in seeing whether the gyre mode, favored at high energy levels, can be realized for Earth by minimal, *reasonable* changes in the parameter values.

For the calculations (variations on A2) f_0 and β are kept fixed and k_β is decreased by raising the heating rate (case A3) and by reducing the drag (case A4). Because of its secondary influence, the static stability is unaltered; but it could be used to provide minor quantitative changes in the results.

a. A3: $H_a^* = 4 \rightarrow 8$, $\tau_D^e = 2.5 \times 10^5$ s

Increasing the heating rate of A2 by a factor of 4 produces a circulation with a stronger (90 m s^{-1}), more meandering jet and the occasional cutoff low-pressure system (Fig. 19). A further doubling of the heating rate boosts the local jet stream to 150 m s^{-1} but *reduces* the mean flow $\bar{u}$, indicating a relative gain in eddy kinetic energy (Fig. 20). Baroclinic activity remains longitudinally localized within the jet stream.

The mean baroclinicity values—40, 53 and 67 K when $H_a^* = 1$, 4 and 8—indicate that the eddy heat transport can cope with a higher heat load and prevent a proportional rise in the temperature distribution. We conclude that the eddies in the class A circulations provide an efficient heat transfer mechanism (Tables 1 and 5).

b. A4: $H_a^* = 4$, $\tau_D^c = 20 \times 10^5$ s

Gyre forms of circulation occur when the energy level is high and the drag low, i.e., when k_β and $k_D \rightarrow 0$. They are virtually excluded from A3 by the strong surface drag. To see whether such a mode could occur on Earth, calculations were made to isolate the minimum value of τ_D at which changes in the circulation pattern could be induced. A transition to gyre form, with jets meandering from pole to equator, was found to occur when $\tau_D \approx 20$ days and $H_a^* = 4$ (Fig. 21). Varying the static stability could reduce the transitional τ_D value to about 10 days.

While such increases in the heating rate could conceivably happen during some epoch, the order-of-magnitude decrease in surface drag needed to change the pattern of climate appears remote; changes to a multi-jet or non-geostrophic mode are more likely.

8. Conclusions

The parameters f_0, β, γ^2, τ_D, H_a, ν, X and Y exert a varying degree of influence on the character of quasi-geostrophic circulations. They do not act in isolation and changes in one can alter the influence of the others. No simple combination describes circulation morphology.

The main roles of the imposed processes are as follows:

1) The Coriolis gradient β and the surface drag act through the transitional wavenumber k_β (the second process indirectly via control of the $\bar{U}$ scale) to determine the barotropic features on the planetary scale, i.e., the number of jets or gyres. The jets are zonal if k_β is large and also regular if k_D is small.

2) The Coriolis term f_0 and static stability parameter γ^2 control the baroclinic eddies and the temperature distribution but have no direct impact on the barotropic features.

3) The heating rate H_a and the internal dissipation also help determine the $\bar{U}$ scale and thence the k_β value.

4) When the scale of the baroclinic eddies approaches that of the domain (X, Y), the spectrum is limited and steady wave flows are preferred.

The calculations indicated that two types of quasi-geostrophic circulation can occur: 1) a jet form when k_β is large (or multiple jets when k_β is very large) and 2) a gyre form when k_β is small and τ_D is large. Large-amplitude meanders occur in the transitional regime between the two extreme states.

Only in the deep meandering flows do the energy conversions differ from the normal energy exchanges of the basic circulation. In such exceptions (A3, A4, D2) the eddies are supported both barotropically by the mean flow ($\{K'\bar{K}\} < 0$) and baroclinically by the potential energy release ($\{P'K'\} > 0$) (Table 5). Mean meridional flows are always weak, particularly when τ_D is large, in keeping with the view that they are needed primarily to balance surface dissipation. The conversion of potential to kinetic energy is strongly localized in cases where Thacker's (1976) criterion $\bar{U} > \sqrt{2}\hat{U}$ is met, even though the model has no imposed longitudinal inhomogeneities. There are no simple parametric preferences for this occurrence.

The existing terrestrial circulation is strongly influenced by effects due to β, τ_D and λ^2: the jet is primarily zonal because k_β ($\sim$4) is large and it meanders because a strong surface drag accentuates the release of potential energy at $k_\rho \sim 6$. The circulation, strongly stable in form, could be close to being a double-jet system, depending on the latitudinal extent available for quasi-geostrophic flow. Although increases in the rotation rate lead to multiple jets within a $Y = 10^4$ km zone, the same result could occur under other circumstances, e.g., by a weakening of the energy level or a decrease in the extent of the tropical regime.

Certain atmospheric "blocking" phenomena ap-

pear to be associated with a splitting of the jet stream and may be a manifestation of a localized transition toward a double-jet system. If this is the case then the onset of *spatial* blocking is due to a change in the *spectral* blocking characteristics of the β and τ_D processes. However, our model excludes certain effects that may be vital to the formation of regional or secondary atmospheric phenomena: spatial and temporal variations in the parameters (cf. Everson and Davies, 1970), and ultralong baroclinically unstable waves (cf. Hirota, 1968).

The connection between the Jovian and terrestrial quasi-geostrophic regimes is simple and direct. The ratio Y/L_β determines the number of jets and this is large for Jupiter mainly because of the great size of that planet. The Jovian jets are more regular than the terrestrial because τ_D and k_ρ are larger. The production of multiple, zonal jets in the terrestrial regime, when Ω and τ_D are altered, verifies this.

REFERENCES

Baines, P. G., 1976: The stability of planetary waves on a sphere. *J. Fluid Mech.*, **73**, 193–213.

Everson, P. J., and D. R. Davies, 1970: On the use of a simple two-level model in general circulation studies. *Quart. J. Roy. Meteor. Soc.*, **96**, 404–412.

Hirota, I., 1968: On the dynamics of long and ultra-long waves in a baroclinic zonal current. *J. Meteor. Soc. Japan*, **46**, 234–249.

Kuo, H-L., 1951: Vorticity transfer as related to the development of the general circulation. *J. Meteor.*, **8**, 307–315.

Lilly, D. K., 1972: Numerical simulation study of two-dimensional turbulence. *Geophys. Fluid Dyn.*, **3**, 289–319.

Merkine, L-O., 1977: Convective and absolute instability of baroclinic eddies. *Geophys. Astrophys. Fluid Dyn.*, **9**, 129–157.

Phillips, N. A., 1954: Energy transformations and meridional circulations associated with simple baroclinic waves in a two-level, quasi-geostrophic model. *Tellus*, **6**, 273–286.

——, 1956: The general circulation of the atmosphere: a numerical experiment. *Quart. J. Roy. Meteor. Soc.*, **82**, 123–164.

Rhines, P. B., 1975: Waves and turbulence on a beta plane. *J. Fluid Mech.*, **69**, 417–443.

Rossow, W. B., and G. P. Williams, 1979: Large-scale motion in the Venus stratosphere. *J. Atmos. Sci.*, **36**, 377–389.

Stone, P. H., 1969: The meridional scale of baroclinic waves. *J. Atmos. Sci.*, **26**, 376–389.

Thacker, W. C., 1976: Spatial growth of Gulf Stream meanders. *Geophys. Fluid Dyn.*, **7**, 271–295.

Williams, G. P., 1978: Planetary Circulations: 1. Barotropic representation of Jovian and Terrestrial turbulence. *J. Atmos. Sci.*, **35**, 1399–1426.

——, 1979: Planetary circulations: 2. The Jovian quasi-geostrophic regime. *J. Atmos. Sci.*, **36**, 932–968.